Nucleic Acids Research, 2024, **52**, 7063–7080
https://doi.org/10.1093/nar/gkae457
Advance access publication date: 29 May 2024
Genomics

PHF2 regulates genome topology and DNA replication in neural stem cells via cohesin

Jia Feng[1], You Heng Chuah[1,2,†], Yajing Liang[1,†], Nadia Omega Cipta[3], Yingying Zeng[3], Tushar Warrier[3], Gamal Ahmed Rashed Elsayed Elfar[3,4], Jeehyun Yoon[1,2], Oleg V. Grinchuk[1,2], Emmy Xue Yun Tay[1], Ker-Zhing Lok[1], Zong-Qing Zheng[1], Zi Jian Khong[3], Zheng-Shan Chong[3], Jackie Teo[3], Emma May Sanford[1,5], Cheryl Jia Yi Neo[1,5], Hsin Yao Chiu[1], Jia Yu Leung[1,3,4], Loo Chien Wang[3], Yan Ting Lim[3], Tianyun Zhao[3], Radoslaw M. Sobota[3], Karen Carmelina Crasta[1,2,3,5], Vinay Tergaonkar[6,7], Reshma Taneja[1,2,5], Shi-Yan Ng[1,3,8], Chit Fang Cheok[3,4], Shuo-Chien Ling[1,5], Yuin-Han Loh[1,3,9] and Derrick Sek Tong Ong[1,2,3,5,8,*]

[1]Department of Physiology, Yong Loo Lin School of Medicine, National University of Singapore, Singapore 117593, Singapore
[2]NUS Centre for Cancer Research Translation Research Program, Yong Loo Lin School of Medicine, National University of Singapore, Singapore
[3]Institute of Molecular and Cell Biology (IMCB), Agency for Science, Technology and Research (A*STAR), Singapore 138673, Singapore
[4]Department of Pathology, Yong Loo Lin School of Medicine, National University of Singapore, National University Hospital, Singapore 119074, Singapore
[5]Healthy Longevity Translation Research Program, Yong Loo Lin School of Medicine, National University of Singapore, Singapore
[6]Department of Biochemistry, Yong Loo Lin School of Medicine, National University of Singapore, 8 Medical Drive, MD7, Singapore 117596, Singapore
[7]Laboratory of NFκB Signalling, Institute of Molecular and Cell Biology (IMCB), Agency for Science, Technology and Research (A*STAR), 61 Biopolis Drive, Proteos, Singapore 138673, Singapore
[8]National Neuroscience Institute, 308433, Singapore
[9]Department of Biological Sciences, National University of Singapore, Singapore 117543, Singapore

[*]To whom correspondence should be addressed. Tel: +65 65163222; Fax: +65 67773271; Email: phsostd@nus.edu.sg
[†]The second and third authors should be regarded as Joint Second Authors.

Abstract

Cohesin plays a crucial role in the organization of topologically-associated domains (TADs), which influence gene expression and DNA replication timing. Whether epigenetic regulators may affect TADs via cohesin to mediate DNA replication remains elusive. Here, we discover that the histone demethylase PHF2 associates with RAD21, a core subunit of cohesin, to regulate DNA replication in mouse neural stem cells (NSC). *PHF2* loss impairs DNA replication due to the activation of dormant replication origins in NSC. Notably, the PHF2/RAD21 co-bound genomic regions are characterized by CTCF enrichment and epigenomic features that resemble efficient, active replication origins, and can act as boundaries to separate adjacent domains. Accordingly, *PHF2* loss weakens TADs and chromatin loops at the co-bound loci due to reduced RAD21 occupancy. The observed topological and DNA replication defects in *PHF2* KO NSC support a cohesin-dependent mechanism. Furthermore, we demonstrate that the PHF2/RAD21 complex exerts little effect on gene regulation, and that PHF2's histone-demethylase activity is dispensable for normal DNA replication and proliferation of NSC. We propose that PHF2 may serve as a topological accessory to cohesin for cohesin localization to TADs and chromatin loops, where cohesin represses dormant replication origins directly or indirectly, to sustain DNA replication in NSC.

Graphical abstract

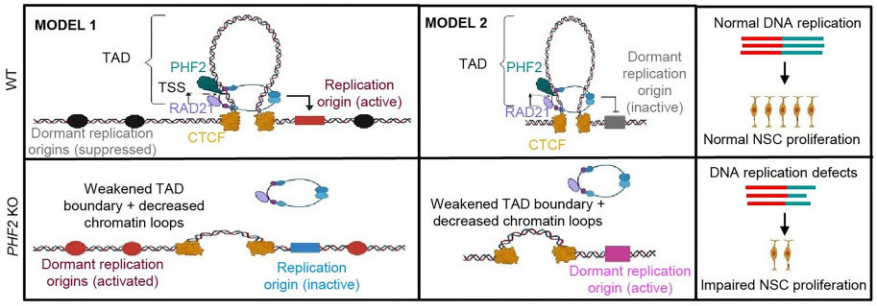

Received: October 19, 2023. **Revised:** April 15, 2024. **Editorial Decision:** May 9, 2024. **Accepted:** May 15, 2024

Introduction

The cohesin complex consists of four major subunits, including SMC1, SMC3, RAD21 and STAG1/2, and forms a ring-like structure that has known roles in mediating sister chromatid cohesion, gene transcription and DNA damage repair (1–4). In addition, cohesin is an important regulator of topologically-associated domains (TADs) (4,5), which are spatially organized DNA domains that are defined by preferential contacts between loci inside the same TAD and insulation from loci in adjacent TADs. In this way, TADs may regulate enhancer-promoter contacts, and hence gene expression. TADs can be studied by genome-wide chromosome conformation capture studies (Hi-C) (6), where many TADs exhibit pronounced 'corner peaks' (or 'loop domains') in Hi-C maps, which report strong interactions between CTCF- and cohesin-bound TAD boundaries (5,7). In the widely accepted 'loop extrusion model', CTCF is thought to bind its cognate sites at loop anchored-TADs in a convergent orientation, followed by the association of cohesin with chromatin that results in DNA loop extrusion (6). Indeed, CTCF or cohesin loss eliminates TADs and well-demarcated loops in Hi-C analysis, indicating their key role in TAD formation and maintenance (8–10).

Beyond gene regulation, TADs can also influence DNA replication in a cohesin-dependent manner (11). The loss of cohesin function (e.g. RAD21 depletion) can disrupt TADs and compromise DNA replication by shifting replication timing or activating dormant origin firing that leads to precocious firing, potentially explaining for how cohesin dysfunction may promote tumorigenesis (12). An enigmatic observation is that while the human genome harbors many replication origins, only a small fraction is actually used for DNA replication at any given time during S phase (13). TAD boundaries often align with replication domains (i.e. genomic regions containing multiple replication origins which coordinately replicate DNA) (14), and highly efficient replication origins preferentially localize to the peripheries or anchors of TADs (15–17), indicating an intimate link between TADs and replication origins. Furthermore, the active replication origins are associated with conducive chromatin architecture (e.g. enriched for active histone marks and nucleosome-depleted regions) (13), and proteomic profiling of chromatin-bound cohesin uncovered transcription factors and chromatin factors (18). Whether epigenetic regulators may regulate TADs via cohesin to mediate DNA replication remains poorly understood.

The plant homeodomain and Jumonji C-containing protein, PHF2, is a histone H3K9 demethylase that recognizes the histone H3K4 di/trimethylation (H3K4me2/3) active transcription marks (19). As an epigenetic regulator that suppresses H3K9me2/3 marks, it plays a pivotal role in tissue homeostasis for adipogenesis, chondrogenesis, osteoblast differentiation and neurogenesis invariably by promoting gene transcription, often in collaboration with tissue-specific transcription factors (20–23). Interestingly, PHF2 can also function as an E3 ubiquitin ligase to degrade SREBP1c, a master transcription factor for lipogenesis, thereby acting as a tumor suppressor in hepatocellular carcinoma cells, indicating that PHF2 can have non-epigenetic roles as well (24). Of relevance to our study, *PHF2* depletion reduces mouse neural stem cell (NSC) proliferation *in vitro*, which is associated with the downregulation of cell cycle genes and increased R-loop formation (presumably due to defective DNA replication) (23). It remains unclear how *PHF2* loss impairs DNA replication in mouse NSC.

In this study, we set out to understand how PHF2 regulates DNA replication in mouse NSC by employing proximity-dependent protein interaction analysis of PHF2; DNA fiber assay of *PHF2* KO mouse NSC, with genetic complementation of wildtype or histone demethylase-dead PHF2; as well as Hi-C and RNA-Seq analyses of *PHF2* KO mouse NSC. These multi-dimensional analyses unveiled an unexpected histone demethylase-independent, cohesin-dependent function of PHF2 in mediating DNA replication by promoting the formation of TADs for the suppression of dormant replication origins in NSC.

Materials and methods

Mouse models

Animal care and experimental procedures were approved by and performed in accordance with guidelines provided by the Institutional Animal Care and Use Committee of the National University of Singapore and complied with the Association for Assessment and Accreditation of Laboratory Animal Care guidelines for animal use. The day of identifying a vaginal plug and the day of birth were designated as embryonic day 0.5 (E0.5), and postnatal day 0 (P0), respectively. All mice used in this study were housed in groups in individually ventilated cages under a 12:12-h light/dark cycle with access to food and water ad libitum. Because there was no apparent gender bias to the observed phenotypes and pathology, female and male mice were included and randomly allocated to experimental groups according to age and genotype.

Nestin-Cre (B6.Cg-Tg(Nes-cre)1Kln/J) mice (JAX stock #003771). *PHF2* floxed mice were obtained from RIKEN BioResource Research Center (BRC). These mice were developed and deposited by Dr Yosuke Okuno and Dr Yuuki Imai at the Institute of Molecular and Cellular Biosciences, The University of Tokyo (20). To generate *Phf2* conditional knockout mice, we mated male Nestin-Cre *Tg*, $PHF2^{flox/+}$ mice with $PHF2^{flox/flox}$ females. Genotyping was performed by PCR using corresponding primers (Supplementary Table S1). All samples were collected at E13.5, P30 and P50.

Immunofluorescence analysis

For tissue preparation, mouse was anaesthetized with isoflurane at the desired time points of E13.5, P30 and P50. The mice were perfused transcardially using phosphate-buffered saline (PBS), followed by 4% paraformaldehyde (PFA) in PBS for fixation. The brain was extracted out of the skull and post-fixed in 4% PFA in PBS overnight. Subsequently, the brain was cryopreserved in 30% sucrose for 48 h and embedded in Surgipath FSC 22 Clear Frozen Section Compound before it was sectioned. Adult brain tissue was sectioned at 25 μm floating in 1× PBS while the embryonic brain tissue was sectioned at 18 μm on slide using a cryostat.

For brain section staining, sections were washed three times, for 5 min each time, with 0.3% Triton X-100 in 1× PBS (PBS-T). Sections were then incubated 30 min at 90°C oven in citrate antigen retrieval buffer at pH 6. After cooling down in room temperature (RT), blocking buffer consisting of 3% bovine serum albumin (BSA) in 1× PBS-T was used for blocking. After blocking at RT for 1 h, the sections were incubated with primary antibodies (Supplementary Table S2) at 4°C overnight. Sections were carefully washed with 0.3% PBS-T three times, for 5 min each time. Secondary antibodies conjugated with Alexa Flour 488, 568, 647 (1:1000, Thermo

Fisher Scientific) and cell nuclei were counterstained with 4′,6-diamidino-2-phenylindole (DAPI) (0.1 ng/μl) (Vector). Sections were then incubated at RT for 2 h in the dark. After incubation, sections were washed with 0.3% PBS-T three times, for 5 min each time, and mounted onto slides with Prolong Gold anti-fade reagent (Thermo Fisher Scientific, P36930).

For immunostaining of cell culture, treated cells were fixed in 4% PFA in room temperature (RT) for 15 min and then permeabilized for 10 min with PBS-Triton X-100 (0.3%). Samples were blocked at room temperature for 1 h in 5% BSA (in PBS with 0.3% Triton X-100). Primary antibodies were incubated in the dark overnight at 4°C. Cells were carefully washed with 0.3% PBS-T three times, for 5 min each time. Secondary antibodies conjugated with Alexa Flour 488, 568, 647 (1:1000, Thermo Fisher Scientific) and cell nuclei were counterstained with 4′,6-diamidino-2-phenylindole (DAPI) (0.1 ng/μl) (Vector). Cells were then incubated at RT for 1 h in the dark, after washed with 0.3% PBS-T three times, for 5 min each time, mounted onto slides with Prolong Gold anti-fade reagent.

EdU (5-ethynyl-2′-deoxyuridine) administration and staining

EdU powder (Toronto Research Chemicals, E932175) was dissolved in sterile 1x phosphate buffered saline (PBS) at the stock concentration of 10mg/ml. For short-term experiment, mice at P30 were injected with EdU at a dosage of 50 mg/kg intraperitoneally for twice during consecutive 4 h. Two hours after the last injection, mice were collected. For EdU labelling of mouse NSCs *in vitro*, the cells were incubated with 10 μM EdU for 1 h at 37°C. For co-staining of EdU with other markers, EdU staining was performed after normal immunofluorescent staining. After washing away the secondary antibodies, cover slips or brain sections were incubated with EdU staining solution (100 mM Tris [pH 7.5], 4 mM $CuSO_4$, 1 mg/ml Sulfo-Cyanide3 Azide (Lumiprobe, A1330) and 100 mM sodium ascorbate) for 1 h at room temperature in dark. After incubation, they were washed thrice with 1× 0.3% PBS-T and mounted onto slides with Prolong Gold anti-fade reagent (Thermo Fisher Scientific, P36930). EdU signal was visualized using red fluorescence at 594 nm.

Image acquisition and quantification

All intact dentate gyrus (DG) images and cell culture images were blindly acquired between control and mutant groups under the same laser power and gain (Zeiss LSM700 inverted confocal microscope 20×, 40×, 63× and 100×). Quantification of images was done on ImageJ and Cellprofiler software.

Cell culture and CRISPR/Cas-9 genome editing

Primary mouse NSC were isolated from the brain cortex of E13.5 embryos. They were cultured on laminin (Gibco™) or Matrigel (Corning®) precoated dishes. The mouse NSC were maintained in NeuroCult Proliferation mouse NSC media (05702, Stem Cell Technologies) supplemented with fibroblast growth factor (FGF) (F0291, Sigma) and epidermal growth factor (EGF) (E4127, Sigma) at 10 and 20 ng/mL, respectively. Human embryonic kidney 293T (HEK-293T) cells were grown in Dulbecco's modified Eagle's medium (DMEM) (Life Technologies) supplemented with 10% fetal bovine serum (FBS) and 1% penicillin–streptomycin solution. The human ESC lines were cultured feeder-free on Matrigel-coated dishes in mTeSR (Stemcell Technologies). Routine passaging was performed every 3 days using ReLeSR (Stemcell Technologies). The following compounds were used in this study: Hydroxyurea (Sigma, H8627-1G) and PHA-767491 (MedChemExpress, HY-13461A).

Guide RNA were designed using the gRNA tool on CRISPick. Genome editing was performed according to Zhangfeng Lab protocol (25), using gRNA targeting exon 2 of PHF2, and mutant clones verified by Western blot. Guide RNA used are listed in Supplementary Table S3.

Lentiviral constructs, shRNAs and molecular cloning

Lentiviruses were generated by co-transfecting HEK293T cells with pMD2.G, pRSV-Rev, pMD-VSVG and overexpression/shRNA plasmids. The media was collected 72-hour post-transfection, concentrated using ultracentrifugation (Optima XL-100K) and the lentiviral particles were resuspended in DMEM/F12. The shRNAs against mouse *RAD21*, shRAD21 #1, (#TRCN0000174832) and shRAD21 #2, (#TRCN0000176084) were purchased from Sigma. The DePinho laboratory provided non-targeting (NT) control shRNA plasmid and pHAGE-PHF2-IRES-GFP vectors. pHAGE-PHF2^{H249A}-IRES-GFP was generated using QuickChange II site-directed mutagenesis kit. BirA*-PHF2 was generated by cloning the ORF into pcDNA3.1-myc-BioID vector. BirA*-PHF2$^{\Delta PHD}$, -PHF2$^{\Delta N}$ and -PHF2$^{\Delta C}$ deletion mutants were generated by amplifying the respective fragments using PCR and subcloned into pcDNA3.1-myc-BioID. BirA*-PHF2$^{\Delta JMJC}$, -PHF2$^{\Delta 56–196}$ and -PHF2$^{\Delta 353–750}$ were generated using Q5® Site-Directed Mutagenesis Kit (New England Biolabs #E0554S) and Gibson Assembly® (New England Biolabs #E2611S) following the manufacturer's instructions. For the overexpression of PHF2 in organoids, pHAGE-PHF2-mCherry and pHAGE-PHF2^{H249A}-mCherry vectors were generated using PCR (Q5 high-fidelity polymerase, NEB) and ligated using Gibson assembly (NEB). All plasmids were verified by Sanger sequencing. The primers used for cloning were listed in Supplementary Table S4.

Cortical spheroid differentiation

Cortical spheroid differentiation was performed according to method described previously (26). Briefly, the human ESC were dissociated using Accutase (Stemcell Technologies) and seeded at 15 000 cells per 96-well on ultra-low attachment U-bottom plates. For neural induction, 0.5μM LDN193189 (Sigma-Aldrich) was used in place of dorsomorphin. N2B27 media (50% DMEM/F12, 50% Neuro medium, 1% L-Glutamax, 1% MEM non-essential amino acids supplemented with 1% N2 supplement, and 2% B27 without Vitamin A supplement) was used throughout the cortical spheroid differentiation with the addition of relevant small molecules.

For genetic complementation experiment, PHF2 KO hESCs were transduced with lentiviruses overexpressing PHF2 or PHF2^{H249A}, along with a mCherry reporter that enables subsequent sorting of the transduced cells.

Proximity-dependent biotinylation (BioID) assay

HEK293T cells were transfected with BioID vector (pcDNA3.1-myc-BioID) expressing BirA*-GFP or -PHF2 respectively. After 48-h post-transfection, cells were replenished with fresh media containing 50 μM biotin (Sigma)

and incubated for 24 h. Transfected cells were lysed in IP lysis buffer and 2–3 mg of lysates were aliquoted for the streptavidin pull down assay. The lysates were incubated with streptavidin agarose beads (Pierce™) overnight at 4°C with gentle rotation. The beads were washed four times with IP wash buffer and streptavidin bound proteins were eluted by boiling the beads with 2× SDS sample loading dye. The samples were analyzed using western blot.

Proteomics sample preparation

PHF2 samples were prepared for proteomics analysis from the streptavidin pull down lysates of HEK293T cells transfected with BirA*-GFP or -PHF2. The streptavidin agarose beads were first washed four times with IP wash buffer, thrice with PBS, and supernatant was removed completely. Beads were then resuspended in 50% (v/v) trifluoroethanol (TFE) in 50 mM triethylammonium bicarbonate (TEAB), pH 8.5 containing 10 mM final concentration of tris(2-carboxyethyl)phosphine (TCEP) and incubated for 20 min at 55°C for disulfide bridge reduction. Samples were cooled to 25°C and alkylated with 55 mM 2-chloroacetamide (CAA) in the dark for 30 min, followed by on-bead digestion with endoproteinase LysC (2 μg final amount) for 3 h and subsequently by trypsin (2 μg final amount) at 37°C overnight. Once completed, beads were removed and the peptides were transferred to new tubes. Digestion was terminated by adding 1% (v/v) final concentration of trifluoroacetic acid (TFA) to the samples, followed by desalting using C18 StageTips. Desalted peptides were dried by centrifugal evaporation, resuspended in 25 μl of TEAB, pH 8.5, and individually labelled using isobaric 6-plex tandem mass tags (TMT6-plex, Thermo Fisher Scientific) at 25°C overnight. TMT-126, 127, 128, 130 and 131 tags were used. After labelling was completed, the reaction was quenched by addition of 30 μl of 1 M ammonium formate, pH 10 into each tube before pooling the samples into a new low-binding 1.5-ml microfuge tube. Pooled sample was desalted and fractionated on a self-packed spin column containing C18 beads (Dr Maisch GmbH) using 14%, 18%, 21%, 24%, 27%, 32% and 60% acetonitrile in 10 mM ammonium formate, pH 10 as the step gradients. Fractions were dried by centrifugal evaporation and further washed and dried twice by addition of 60% acetonitrile in 0.1% formic acid to further remove residual ammonium formate salts.

BioID interactomics by tandem mass spectrometry analysis

Dried fractions were resuspended in 30 μl of 2% (v/v) acetonitrile containing 0.06% (v/v) trifluoroacetic acid and 0.5% (v/v) acetic acid and transferred to an autosampler plate. Online chromatography was performed in an EASY-nLC 1000 (Thermo Fisher Scientific) liquid chromatography system using a single-column setup and 0.1% formic acid in water and 0.1% formic acid in 99% acetonitrile as mobile phases. Fractions were injected and separated on a reversed-phase C18 analytical column (Easy-Spray, 75 μm inner diameter × 50 cm length, 2 μm particle size, Thermo Fisher Scientific) maintained at 50°C and using a 2–33% (v/v) acetonitrile gradient over 55 min, followed by an increase to 45% over the next 5 min, and to 95% over 5 min. The final mixture was maintained on the column for 4 min to elute all remaining peptides. Total run duration for each sample was 70 min at a constant flow rate of 300 nl/min.

Data were acquired using an Q Exactive HFX mass spectrometer (Thermo Fisher Scientific) using data-dependent mode. Samples were ionized using 2.1 kV and 300°C at the nanospray source. Positively-charged precursor signals (MS1) were detected using an Orbitrap analyzer set to 60000 resolution, automatic gain control (AGC) target of 3 000 000 ions, and maximum injection time (IT) of 50 ms. Precursors with charges 2–7 and having the highest ion counts in each MS1 scan were further fragmented using higher-energy collision dissociation (HCD) at 36% normalized collision energy. Fragment signals (MS2) were analysed by the Orbitrap analyzer at a resolution of 7500, AGC of 100 000 and maximum IT of 100 ms. Precursors used for MS2 scans were excluded for 30 s to avoid re-sampling of high abundance peptides. The MS1–MS2 cycles were repeated every 40 MS2 scans until completion of the run.

Proteomics data analysis

Proteins were identified using Proteome Discoverer™ (v2.4, Thermo Fisher Scientific). Raw mass spectra were searched against human primary protein sequences retrieved from Swiss-Prot (11 June 2019). Carbamidomethylation on Cys and TMT6-plex on Lys and N-terminus were set as a fixed modification; deamidation of asparagine and glutamine, acetylation on protein N-termini, methionine oxidation, and biotinylation of lysine or peptide N-termini were set as dynamic modifications for the search. Trypsin/P was set as the digestion enzyme and was allowed up to three missed cleavage sites. Precursors and fragments were accepted if they had a mass error within 10 ppm and 0.06 Da, respectively. Peptides were matched to spectra at a false discovery rate (FDR) of 1% (strict) and 5% (relaxed) against the decoy database and quantitated using TMT6-plex method. Search result was exported and further processed for differential analysis using an in-house R-based script that was built upon the *limma* package from Bioconductor. Proteins with differential expression were identified by comparing the treatment with the control with a $\log_2$ fold change ($\log_2$ FC) cutoffs of 1 and –1 and *P*-value adjusted using the Benjamini–Hochberg method of <0.05 as significant hits.

Immunoblotting and immunoprecipitation (IP)

Immunoblotting was performed using standard procedures and the chemiluminescent images were obtained using the ChemiDoc imaging system (BioRad) and quantified using the ImageJ software. Antibodies and horseradish peroxidase (HRP)-conjugated secondary antibodies used are listed in Supplementary Table S2. To analyze protein interactions, equal amount of cell lysates was used for the control and target IP and incubated with primary antibody at 4°C overnight. Next, equilibrated Protein A/G beads (Thermo #WC322042) were added to precipitate the immune complexes for four hours at 4°C on the following day. After three washes with washing buffer (50 mM Tris pH7.5, 150 mM NaCl, 1% Triton X-100), the precipitated proteins were eluted in a denaturing 2× sodium dodecyl sulfate (SDS) sample buffer and resolved using sodium dodecyl sulfate-polyacrylamide gel electrophoresis (SDS-PAGE). Western blot analysis of PHF2 and its identified interactors were used to confirm that the IP experiment is successful.

Public datasets and data analyses

ChIP-Seq datasets for PHF2 (GSM346270 (4)) and RAD21 (GSE48938 (5)) in NSCs were downloaded using the sra-toolkit (https://github.com/ncbi/sra-tools/wiki) and converted into fastq files. The fastq files were mapped to the mm10 genome assembly using the STAR aligner (6) with the –alignIntronMax option being set to 1, and the –alignEndsType option being set to EndToEnd, to ensure ChIP-Seq compatibility. The –outFilterMultimapNMax option was set to 500, in order to include and retain repeats and multi-mapped regions of the genome. The MACS2 (7) callpeak option was used to call peaks for the libraries. Input DNA libraries were used as control files by using the -c option for the callpeak command. The output SAM files from the STAR aligner were sorted and indexed using samtools (8), and converted into bigwig files for visualization, by using the bamCoverage option of the deeptools (9) suite. The deeptools software suite was used for plotting heatmaps for the ChIP-Seq data. A matrix for the data was created by using the computeMatrix function with the scale-regions and –skipZeros options. Using the matrix, enrichment heatmaps were plotted with the plotHeatmap function.

For chromatin segmentation state analysis, multiple neural stem cell (NSC) ChIP-Seq libraries were downloaded from GEO using the sra-toolkit—H3K27Ac (GSM2406791 (11)), H3K4me3 (GSM1516102, GSM1516103 (12)), H3K27me3 (GSM1516094, GSM1516095 (12)), CTCF (GSM7134806 (27)), RING1B (GSM5732313 (28)), EZH2 (GSM786030 (29)). All ChIP-Seq datasets were processed using the STAR aligner and were mapped to the mm10 genome. The ATAC-Seq dataset was mapped to the mm10 genome assembly using bowtie-2. The SAM output files were converted to BAM and were sorted and indexed, by using samtools. The BinarizeBed command from the ChromHMM (14) toolkit was used to develop a chromatin segment state model using a Hidden Markov Model pipeline. Finally, the LearnModel command from ChromHMM was utilized to segment the NSC genome into 20 distinct states based on enrichment, expression and accessibility profiles derived from the analyzed datasets.

DNA fiber labelling

DNA fiber assay was performed according to methods described previously (30). Briefly, nascent DNA were labeled with 25μM IdU (17125, Sigma) and 250μM CldU (c6891, Sigma) nucleotide analogs for 20 minutes each, in order. The cell pellets were collected and lysed on a microscope slides, DNA spreading was performed by tilting the slides at an angle of 25–40°C for 3–5 min. The spread DNA is dried at room temperature for 20 min and fixed in Carnoy's fixative (3:1 methanol:glacial acetic acid). The DNA fibers are immunolabeled following the immunostaining of cell culture protocol. Confocal 63× images are acquired for analysis. Quantification of DNA fibers is performed using ImageJ software, with fork speed measured by dividing the length of both tracts by the labeling time. The values are converted from micrometers into kilobases. This method enables accurate quantification of DNA fiber dynamics in cells.

For CDC7 inhibitor rescue and PHF2 and RAD21 co-depletion experiments, cells are labeled with CldU for 15 min followed by IdU. The Axioimager Z1 microscope (Zeiss) was utilized to acquire images. The active origin percentages were quantified by calculating the number of active origins (green–red–green) tracts relative to all replicative tracts in one image ($n > 5$).

Chromatin isolation for analysing chromatin-bound pre-RC complex

The isolation of chromatin extracts was performed as described previously (31). Briefly, mouse NSCs were resuspended (4×10^7 cells/ml) in buffer A (10 mM HEPES, [pH 7.9], 10 mM KCl, 1.5 mM $MgCl_2$, 0.34 M sucrose, 10% glycerol, 1 mM DTT, 0.1% Triton X-100) supplemented with protease inhibitor cocktails (Roche). The cells were incubated for 5 min on ice, followed by low-speed centrifugation at 1300g for 4 min at 4°C. The pellet was washed once with buffer A, resuspended in buffer B (3 mM EDTA, 0.2 mM EGTA, 1 mM DTT) supplemented with protease inhibitor cocktails, followed by 30 min incubation on ice. The samples were centrifuged at 1700g for 5 min, 4°C and the pellets were washed once with buffer B. Finally, the pellets were resuspended in Laemmli buffer, followed by brief sonication using the Bioruptor Pico (Diagenode) to obtain the chromatin extracts. To prepare the total cell extracts (TCE), the cells were resuspended in Laemmli buffer, followed by brief sonication.

Nuclear abnormality scoring

Wild-type and *PHF2* KO mouse NSCs were seeded on cover slips, fixed with 4% PFA and were stained with DAPI. Cover slips were mounted into slides and images were acquired using the Zeiss LSM700 inverted confocal microscope. Cells were categorized based on specific types of nuclear abnormality. Micronucleated cells may contain one or multiple nuclear compartments that are external to the primary nucleus. External nuclear compartments that are less than 1/3 of the size of the main nucleus are considered as micronucleus. Multinucleated cells contain multiple nuclear compartments that are of about equal sizes. These cells may also contain micronuclei. The % multi-nucleated or micro-nucleated cells were calculated based on the ratio of the number of multinucleated/micro-nucleated cells over total cells per field. Approximately 40–50 fields were analysed per condition.

RNA-seq analysis

Total RNA from primary wild-type, *PHF2* KO mouse NSCs, mouse NSC transduced with non-targeting shRNA, and shRAD21 (shRAD21#1 and shRAD21 #2) were isolated using RNeasy® Mini kit (Qiagen) and sent to NovogeneAIT (Singapore) for RNA-Seq analysis. Transcriptomic sequencing (RNA-Seq) was performed on the Illumina HiSeq platform according to the standard paired-end protocol. RNA-seq data quality was monitored via FASTQC package (https://www.bioinformatics.babraham.ac.uk/projects/fastqc/). Adapters and overrepresented sequences have been removed using cutadapt software (https://cutadapt.readthedocs.io/en/stable/). Further reads preprocessing was performed by Trim Galore (https://www.bioinformatics.babraham.ac.uk/projects/trim_galore/) with default parameters. Mapping of RNA-seq reads was done using bowtie2 against mouse genome mm10 with default parameters for RNA-seq data. RSEM software was used to quantify the gene-level expression. GO term annotation with differentially expressed genes (DEGs) was performed using the software Metascape (https://metascape.org/gp/index.html#/main/step1).

ChIP-qPCR analysis

For chromatin immunoprecipitation (ChIP) assays, cells were cross-linked with 1% formaldehyde for 10 minutes in the culture medium at 37°C. Fixation was stopped by adding 0.125 M glycine. Cells were rinsed with PBS and lysed in 1% SDS lysis buffer (1% SDS; 10 mM EDTA pH8.0; 50 mM Tris–HCl pH 8.1). Chromatin sonication was performed in a Bioruptor sonicator (Diagenode) before immunoprecipitation to produce DNA fragments of 200 – 1000 bp in length. 10% of sample was kept aside as input. Chromatin was diluted 10-fold with ChIP dilution buffer (0.01% SDS, 1.1% Triton X-100, 1.2 mM EDTA, 16.7 mM Tris pH 8.1, 167 mM NaCl), pre-cleared and immunoprecipitated with the respective antibodies (Supplementary Table S2). After washes, and reverse crosslinking, samples were treated with proteinase K and DNA was purified using phenol-chloroform- isoamyl alcohol (Sigma). Finally, ChIP DNA was analyzed by qPCR with SYBR Green (Roche) in a LightCycler 480 PCR system (Roche) using primers indicated in Supplementary Table S5. The percentage of input was used for the quantification of the immunoprecipitated material with respect to the total starting chromatin.

Hi-C library preparation

HiC libraries were prepared according to the Dovetail Topolink kit protocol version 1.2 (Cantata Bio). Briefly, 1 million cells were crosslinked with disuccinimidyl glutarate and formaldehyde. Next, the nuclei were extracted and the chromatin was enzymatically fragmented. The profile of chromatin fragmentation was quality-controlled by Bioanalyzer DNA high sensitivity assay (Agilent Technologies). Following this, 3 ng of fragmented chromatin was proximity ligated on chromatin capture beads. The resulting chromatin was subjected to library preparation mix 1 and 2, then reverse crosslinked and quantified using Qubit dsDNA HS kit (Thermo Fischer). The DNA yield was split evenly into 4 reactions, and each was prepared into dual-indexed HiC library using library prep mix 3 and 4. Each library was sequenced to approximately 200 million paired-end reads on NovaSeq6000 platform (Illumina).

Hi-C data analysis

Hi-C reads were mapped to the mouse reference assembly mm9 using bwa mem. Alignments were parsed and pairs were classified and deduplicated using pairtools (https://github.com/mirnylab/pairtools) package to generate the .bam and .pairs files. Output files containing all valid pairs were used for downstream analyses. Valid pairs were converted to .hic file using the Juicer (32) (https://github.com/aidenlab/juicer) package or .cool file using the cooler (33) (https://github.com/open2c/cooler) package. Topologically associated domains were called using Juicer tools with arrowhead command in 25 kb resolution. Chromatin loops for each sample and differential chromatin loops between WT and Phf2-KO sample were identified using Mustache (34) (https://github.com/ay-lab/mustache) at 10kb resolution. Pile-up plots at chromatin loops and TADs were generated by coolpup.py (35). The average profile of insulation score around ChIP-seq peaks were performed using GENOVA (36).

Statistical analysis

Quantitative data were expressed as means and standard deviation (SD) or mean and standard error means (SEM), as indicated in the figure legends. The significance of differences between groups was assessed using two-tailed *t*-test. Significance was reported at $P < 0.05$. All statistical analyses were performed in GraphPad Prism software, R packages ggplot2, ggpubr as well as seaborn package from visualization library matplotlib (python) were used for graphs plotting.

Results

PHF2 proximity proteomics identify new interactions between PHF2 and cohesin complex

To understand how PHF2 may play a role in DNA replication, we fused PHF2 (and a GFP control) to a promiscuous biotin ligase BirA* along with a myc-tag to define the PHF2 interactome (includes weak/transient and stable interactors, as well as direct and indirect interactors) in 293T cells. The PHF2 proximal proteins were labeled in their native environment with biotin, and biotinylated proteins were enriched and then identified by mass spectrometry. This revealed the enrichment of about 90 proteins in the PHF2 versus GFP proximal proteomes (FC > 2, FDR < 0.05) that have roles in the DNA damage response, and ribosomal protein and RNA biogenesis pathways (Figure 1A and Supplementary Figure S1A). Among the PHF2 proximal proteins, the cohesin complex caught our attention as four out of the five subunits of the cohesin complex (RAD21, STAG1, STAG2 and SMC3) were among the top hits, consistent with the enrichment of PHF2 interactors in the 'cohesin loading onto chromatin' Reactome pathway (Figure 1A and Supplementary Figure S1A and B). We validated the enrichment of RAD21, STAG1, STAG2 and SMC3 in the PHF2 proximal proteome, and found that only RAD21 binds to PHF2 in myc immunoprecipitation experiments (Figure 1B and C). Furthermore, PHF2 deletion mutant analysis identified amino acids 353–750 of PHF2 to be crucial for its interaction with RAD21 (Figure 1D–F). Importantly, the endogenous PHF2-RAD21 protein interaction could also be detected using mouse NSC lysates (Figure 1G). We conclude that PHF2 specifically associates with RAD21 (likely as a cohesin complex) in 293T cells and mouse NSC, and that this interaction may mediate DNA replication.

Characterization of NSC-specific *PHF2* cKO mouse embryo

Previously, it was reported that the shRNA-mediated depletion of *PHF2* decreased mouse NSC proliferation *in vitro*, which was linked to an increase in R-loops (a marker of replication stress) albeit via poorly understood mechanisms (23). Thus, we generated a NSC-specific *PHF2* conditional knockout (cKO) mouse model (*Nes-Cre;PHF2*$^{f/f}$; *≪f≫/flox*) to audit the changes in the NSC pool *in vivo*, and derive embryonic NSC from this model for our downstream investigation of PHF2 in DNA replication. To this end, we crossed the *Nes-Cre;PHF2*$^{f/+}$ mice with *PHF2*$^{f/f}$ mice (20) to specifically delete *PHF2* in the NSC. The resulting pups showed the expected Mendelian ratio of 1:1:1:1 for the respective genotypes (Supplementary Figure S2A). We also confirmed that PHF2 expression was greatly diminished in the NSC of P50 *PHF2* cKO mouse brains, indicating efficient *PHF2* KO (Supplementary Figure S2B). As expected, there was a

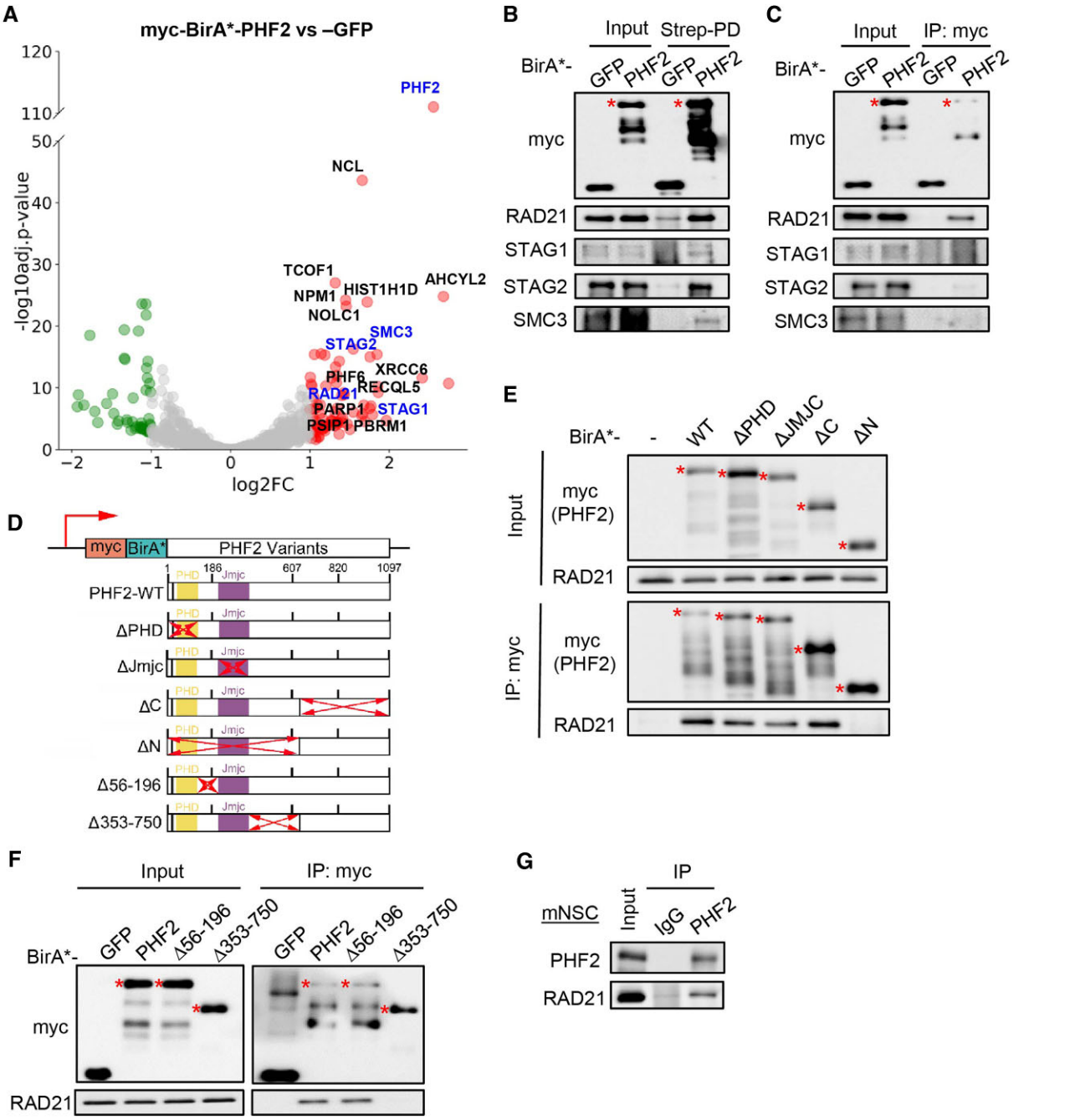

Figure 1. PHF2 proximity proteomics identify new interactions between PHF2 and cohesin complex. (**A**) Volcano plot showing the proteins which were enriched in the PHF2 vs GFP proximal proteomes. (B-C) Western blot analysis of cohesin complex subunits (RAD21, STAG1, STAG2 and SMC3) in the streptavidin pulldown lysates (**B**) or myc immunoprecipitates (IP) (**C**) of HEK293T cells transfected with myc-BirA*-PHF2 or GFP. The correct PHF2 bands are indicated with red *. (**D**) Structure of human PHF2 protein and the variants used in the protein interaction analysis. (**E, F**) Western blot analysis of RAD21 in the myc IP using lysates of HEK293T cells that were transfected with the indicated PHF2 constructs. The correct PHF2 bands are indicated with red *. **(G)** Western blot analysis of RAD21 protein in the PHF2 IP using mouse NSC lysates.

significant reduction in the number of total (Sox2$^+$) (∼17%) and proliferating mouse NSC (Sox2$^+$EdU$^+$) (∼18%) upon *PHF2* loss in the E13.5 mouse brains (Figure 2A–C). Concordantly, we observed a decrease in the number of total (Tbr2$^+$) (∼18%) and proliferating intermediate neural progenitors (Tbr2$^+$EdU$^+$) (∼16%) (Figure 2D–F), which resulted in reduced neurogenesis as assessed by cortical plate thickness (based on TuJ1$^+$ neurons) (∼18%) in *PHF2* cKO embryonic brain (Figure 2A, G). There was also significantly more NSC with DNA damage (≥3 γH2AX foci) and increased genomic instability (as reflected by multi-nucleated cells and micronuclei) in the *PHF2* KO vs intact NSC (Figure 2H and I; and Supplementary Figure S2C–E). Taken together, we validated that *PHF2* loss leads to a NSC proliferation defect that consequently impairs neurogenesis *in vivo*, and is linked to heightened DNA damage and genomic instability, hence justifying the use of the *PHF2* KO mouse NSC for our subsequent experiments.

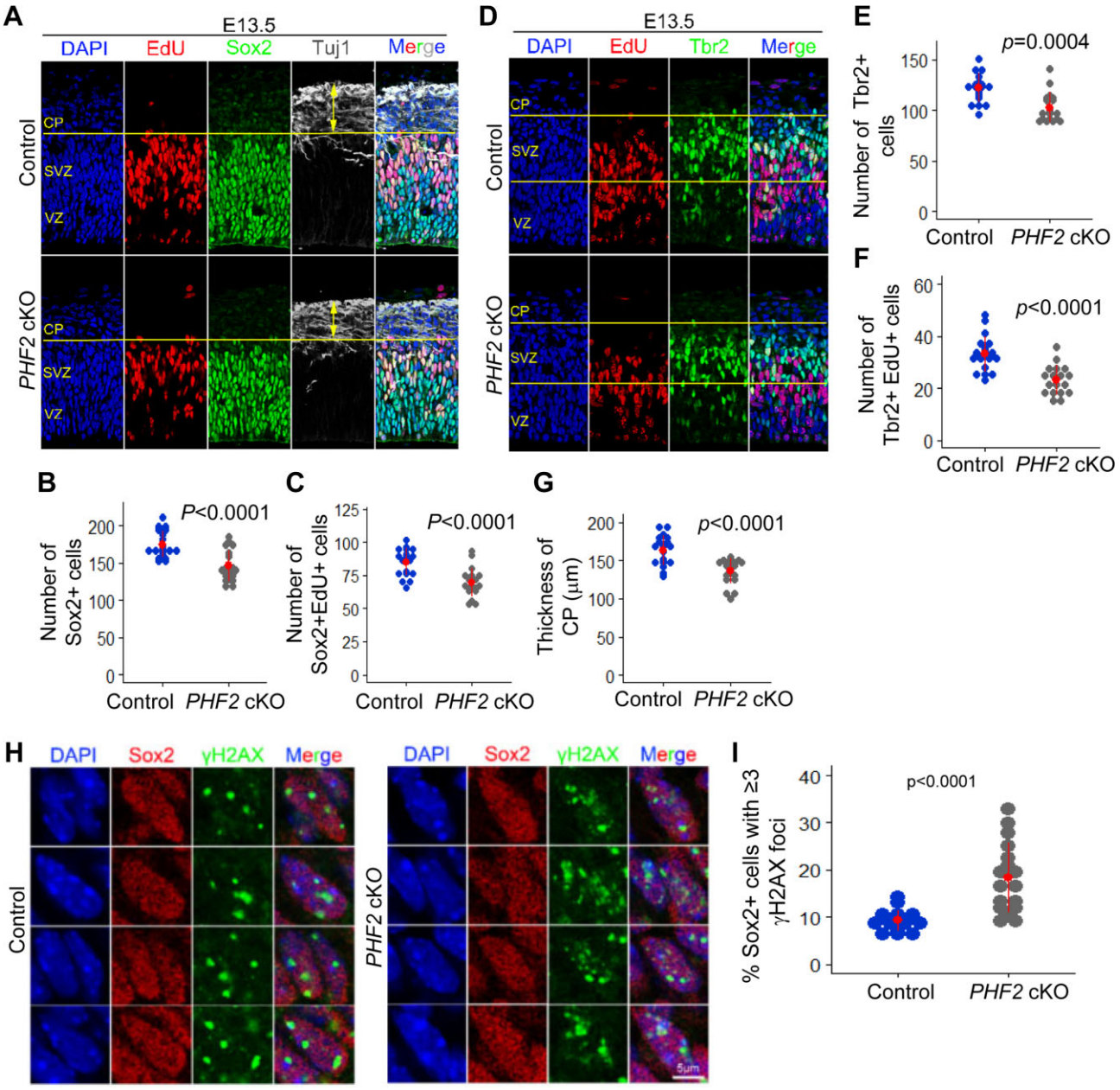

Figure 2. Characterization of NSC-specific *PHF2* cKO mouse embryo. (**A**) Coronal cortical sections of E13.5 control and *PHF2* cKO embryonic brains stained for Sox2, Tuj1 and EdU, 2 hours post EdU administration. Thickness of cortical plates is marked by Tuj1 staining as shown by the yellow double-sided arrows. (**B, C**) Quantification of total ($Sox2^+$) and proliferating ($Sox2^+EdU^+$) mouse NSCs in the neocortices of E13.5 *PHF2* cKO embryonic brains when compared to controls ($n = 5$ mice, 3–4 sections per brain). (**D**) Coronal cortical sections of E13.5 control and *PHF2* cKO embryonic brains stained for intermediate progenitor cells (IPCs) marker Tbr2 and proliferating cell tracing marker EdU. Brains were collected 2 h following EdU injection. (**E, F**) Quantification of intermediate progenitor cells ($Tbr2^+$) and proliferating intermediate progenitor cells ($Tbr2^+EdU^+$) in the neocortices of E13.5 *PHF2* cKO embryos compared to controls ($n = 5$ mice, 3–4 sections per brain). **(G)** The measurement of cortical plate thickness in *PHF2* cKO embryonic brains compared to controls ($n = 5$, 3–4 sections per brain). (**H**) Coronal cortical sections of E13.5 control and *PHF2* cKO embryonic brains stained for Sox2 and γH2AX. (**I**) Quantification of γH2AX foci in mouse NSC ($Sox2^+$) in the neocortices of E13.5 *PHF2* cKO embryonic brains when compared to controls ($n = 5$ mice, 3–4 sections per brain).

PHF2 mediates DNA replication in mouse NSC, in a histone demethylase-independent manner

Next, we employed the DNA fiber assay to directly assess DNA replication defects in *PHF2* KO mouse NSC, and asked if this was dependent on PHF2's histone demethylase activity. In this experiment, we pulse labeled wildtype, *PHF2* KO, *PHF2* KO with re-expression of PHF2 (i.e. *PHF2* KO + PHF2), or *PHF2* KO with re-expression of $PHF2^{H249A}$ (i.e. *PHF2* KO + H249A) mouse NSC with IdU, followed by CldU, and then performed DNA fiber assay to evaluate the length of the CldU tracks and fork symmetry (Figure 3A–C). The H249A mutant is a well-established PHF2 variant that has lost its histone demethylase activity for gene regulation (24,37). There was a significant reduction in the replicative DNA fiber length in *PHF2* KO mouse NSC, which was unexpectedly reversed upon the re-expression of PHF2 or H249A (Figure 3D, E). To detect stalled or collapsed forks, we analyzed fork symmetry between the first and second pulses in the IdU/CldU dual

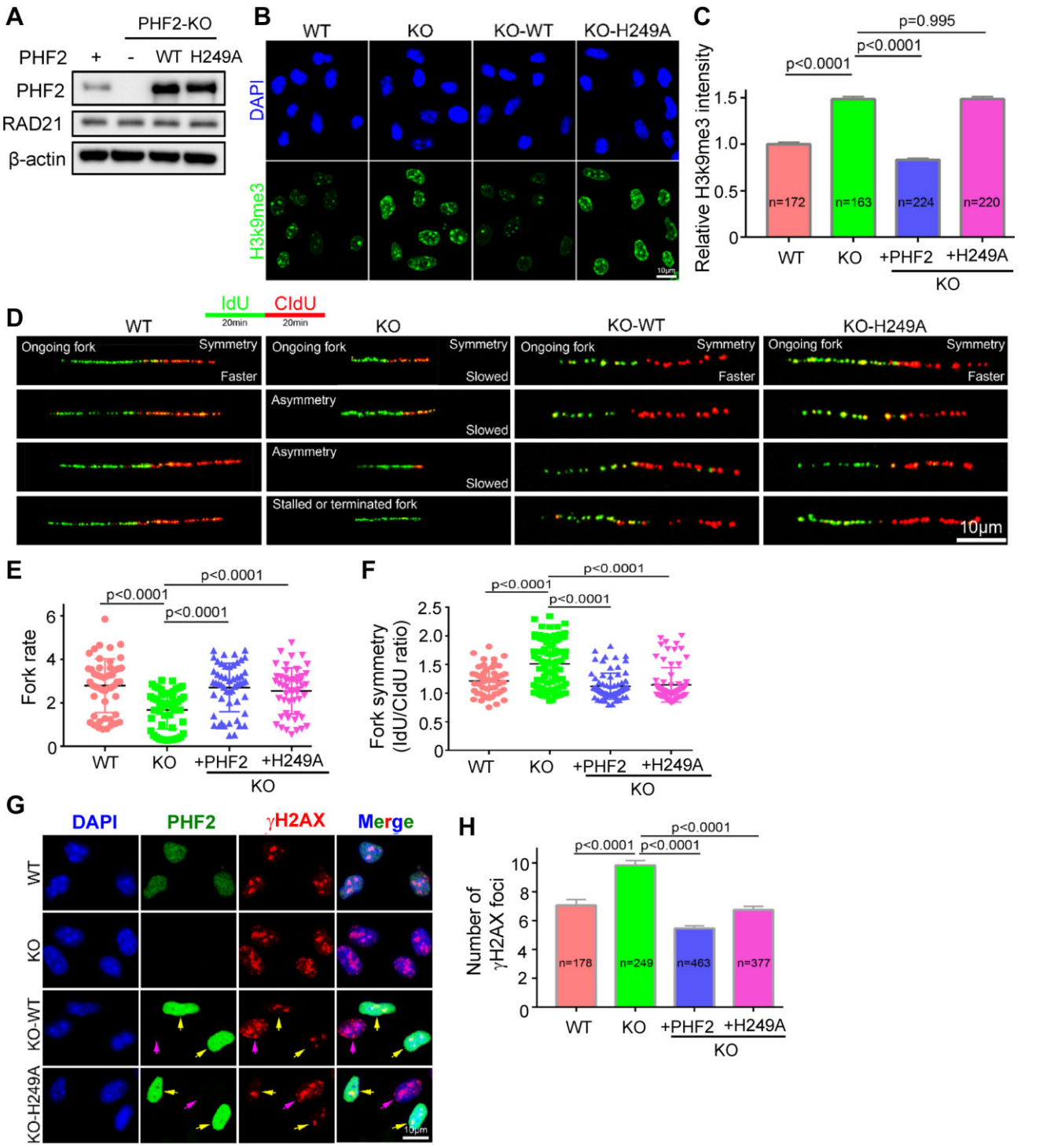

Figure 3. PHF2 mediates DNA replication in mouse NSC, in a histone demethylase–independent manner. (**A**) Western blot analysis of PHF2 and RAD21 in *PHF2* intact, *PHF2* KO, *PHF2* KO + PHF2, and *PHF2* KO + H249A mouse NSC. β-actin serves as loading control. (**B, C**) Confocal images and quantification of the relative intensity of H3K9me3 in *PHF2* intact, *PHF2* KO, *PHF2* KO + PHF2, and *PHF2* KO + H249A mouse NSC. (**D**) Representative confocal images of DNA fiber assay of *PHF2* intact, *PHF2* KO, *PHF2* KO + PHF2, and *PHF2* KO + H249A mouse NSC. (**E**) Quantification of fork rate of *PHF2* intact, *PHF2* KO, *PHF2* KO + PHF2, and *PHF2* KO + H249A mouse NSC. Fork rate (kb/min) was determined by measuring CldU (red) track length ($n = 100$) over 20 minutes. (**F**) Quantification of fork symmetry of *PHF2* intact, *PHF2* KO, *PHF2* KO + PHF2 and *PHF2* KO + H249A mouse NSC. Fork symmetry was determined by measuring the ratio of IdU (green) and CldU (red) track length ($n = 100$). (**G, H**) Confocal images and quantification of γH2AX foci in *PHF2* intact, *PHF2* KO, *PHF2* KO + PHF2, and *PHF2* KO + H249A mouse NSC.

labeled DNA fibers, and found asymmetric fork progression in *PHF2* KO mouse NSC, which was again rescued upon the re-expression of PHF2 or H249A (Figure 3F). Notably, these changes tracked closely with the levels of γH2AX in mouse NSC of the respective genotypes, consistent with replication stress-induced DNA damage in the absence of *PHF2* (Figure 3G, H). As a positive control, we also conducted DNA fiber assay with *RAD21* depleted mouse NSC. As expected, *RAD21* loss results in a significant decrease in replicative DNA fiber length and increased asymmetric fork progression in mouse NSC (Supplementary Figure S3A–D). Collectively, we find that *PHF2* mediates DNA replication in mouse NSC, in a histone demethylase-independent manner.

DNA replication defect in *PHF2* KO NSC is due to the activation of dormant origins

To identify the cause of DNA replication defect, we first compared the levels of chromatin-bound pre-replication complex (pre-RC) proteins, including MCM2, CDC6 and ORC2, in the chromatin extracts of WT, *PHF2* KO, *PHF2* KO + WT and *PHF2* KO + H249A NSCs. The levels of chromatin-bound MCM2, CDC6 and ORC2 were visibly higher in *PHF2* KO than WT NSCs, and there was a clear rescue of chromatin-bound MCM2 and CDC6 with the re-expression of WT or H249A PHF2 in the *PHF2* KO cells (Figure 4A). These results corroborate with transient EdU incorporation assay wherein *PHF2* KO NSCs exhibit greater EdU incorporation than their WT counterpart, which was again reversed upon WT or H249A PHF2 overexpression (Figure 4B, C). The increased chromatin-bound MCM proteins and EdU incorporation in *PHF2* KO NSC are signs of dormant replication origin firing (12,38). In contrast, we found that *RAD21* depletion reduced the levels of chromatin-bound (and total) pre-RC proteins (Supplementary Figure S3E). This aligns with significantly lower EdU incorporation in *RAD21* KD than intact NSC (Supplementary Figure S3F, G). There was no change in p-CHK1 levels upon *RAD21* silencing in NSC (Supplementary Figure S3A). The discrepancy in chromatin-bound pre-RC protein and EdU labelling analyses between *PHF2* KO and *RAD21* KD NSC may be explained by the diverse roles of RAD21 (and cohesin) in genome topology, chromatid cohesion, DNA damage response and gene regulation (39–41), which may directly or indirectly affect DNA replication dynamics.

If the activation of dormant origins were the primary cause for DNA replication defect in *PHF2* KO NSC (since this would deplete dNTP pools), we reasoned that the decreased replicative DNA fiber length should be rescued upon CDC7 kinase inhibitor (PHA-767491, which would inhibit MCM helicase and origin firing) treatment (42). Intriguingly, CDC7 kinase inhibitor treatment almost completely rescued the reduced replicative DNA fiber length of *PHF2* KO cells (Figure 4D–F). In addition, we quantified % of active origins and as expected, CDC7i treatment reduced active origins in both WT and *PHF2* KO mouse NSC (Figure 4G). Notably, *PHF2* KO mouse NSCs show a greater % of active origins than the WT mouse NSCs, suggesting that *PHF2* loss results in the activation of extra-origins (Figure 4G). Since intra-S phase checkpoint suppresses the activation of dormant origins, we also assessed the levels of p-CHK1 as a readout for replication defect-associated checkpoint. There was no change in p-CHK1 levels in *PHF2* KO versus WT NSCs, which aligns with the activation of dormant origins in *PHF2* KO NSCs (Figure 4H). In addition, we performed DNA fiber assay of *PHF2* KO NSC, with or without *RAD21* depletion, to understand if this would lead to an additive/synergistic effect in impairing DNA replication. The replicative DNA fiber length in *RAD21* depleted, *PHF2* KO NSC was significantly lower than *PHF2* KO cells (Supplementary Figure S3H-J). Importantly, the replicative DNA fiber length upon combined loss of *PHF2* and *RAD21* was modestly lower than that with *RAD21* depletion alone (i.e. no additive effect). If PHF2 were to regulate DNA replication in RAD21-dependent and independent manners, one would expect the replicative DNA fiber length of *PHF2* KO + *RAD21* KD NSC to be much lower than that of *RAD21* KD NSC. Thus, our results support the idea that PHF2 is unlikely to regulate DNA replication in a RAD21-independent manner. We conclude that *PHF2* loss activates dormant origin firing that impairs DNA replication in NSC.

PHF2 facilitates RAD21 binding to PHF2/RAD21 co-bound sites, which are CTCF-enriched and resemble efficient, active replication origins

Given that PHF2 may serve to suppress dormant origin firing and associates with RAD21, we sought to characterize the genomic and epigenomic features of the PHF2/RAD21 co-bound regions so as to understand their potential connection with replication origins (Figure 5A, B). There were 816 co-bound peaks among the 5989 PHF2 and 18406 RAD21 unique peaks, (∼4.4% of cohesin-bound sites), and the vast majority of these co-bound peaks are localized to the transcription start site (TSS), which aligns with the view that replication origins/initiation sites overlap with TSS and there is a strong correlation between origin efficiency and their proximity to the nearest TSS (Figure 5C, D) (43). Using HOMER analysis, we identified CTCF-associated motif as the top motif for the co-bound and RAD21-only sites, but not PHF2-only sites (Supplementary Figure S4A). We also calculated the fraction of co-bound, PHF2-only and RAD21-only peaks that overlap with CTCF peaks. Notably, there was a larger fraction of co-bound (∼0.63) and RAD21-only (∼0.61) peaks that overlapped with CTCF than that of PHF2-only (∼0.20) (Figure 5E). Thus, the co-bound sites are more highly enriched for CTCF than PHF2-only sites. Next, we performed ChromHMM analysis of PHF2, RAD21, and CTCF, along with histone modifications that are associated with replication origins, including H3K27ac, H3K4me3 and H3K27me3 (a facultative heterochromatin mark along with its associated chromatin factors, EZH2 and RING1B) (44), to compare PHF2/RAD21- vs PHF2-only-associated genomic segments. Interestingly, the co-bound genomic segments are strongly correlated with H3K27me3, EZH2 and RING1B, as well as to a lesser extent with H3K27ac and H3K4me3 (particularly in state 2), which were previously linked to replication origins (Figure 5F) (43). In contrast, the PHF2-linked genomic segments are strongly correlated with H3K27ac and H3K4me3, but to a lesser extent with H3K27me3, EZH2 and RING1B (particularly in state 15). Therefore, the co-bound segments may resemble class 3 origins that are the most efficient and linked to open chromatin and polycomb protein-enriched regions (44).

To address how *PHF2* loss may interfere with the function of RAD21 (and cohesin), we analysed the protein levels of

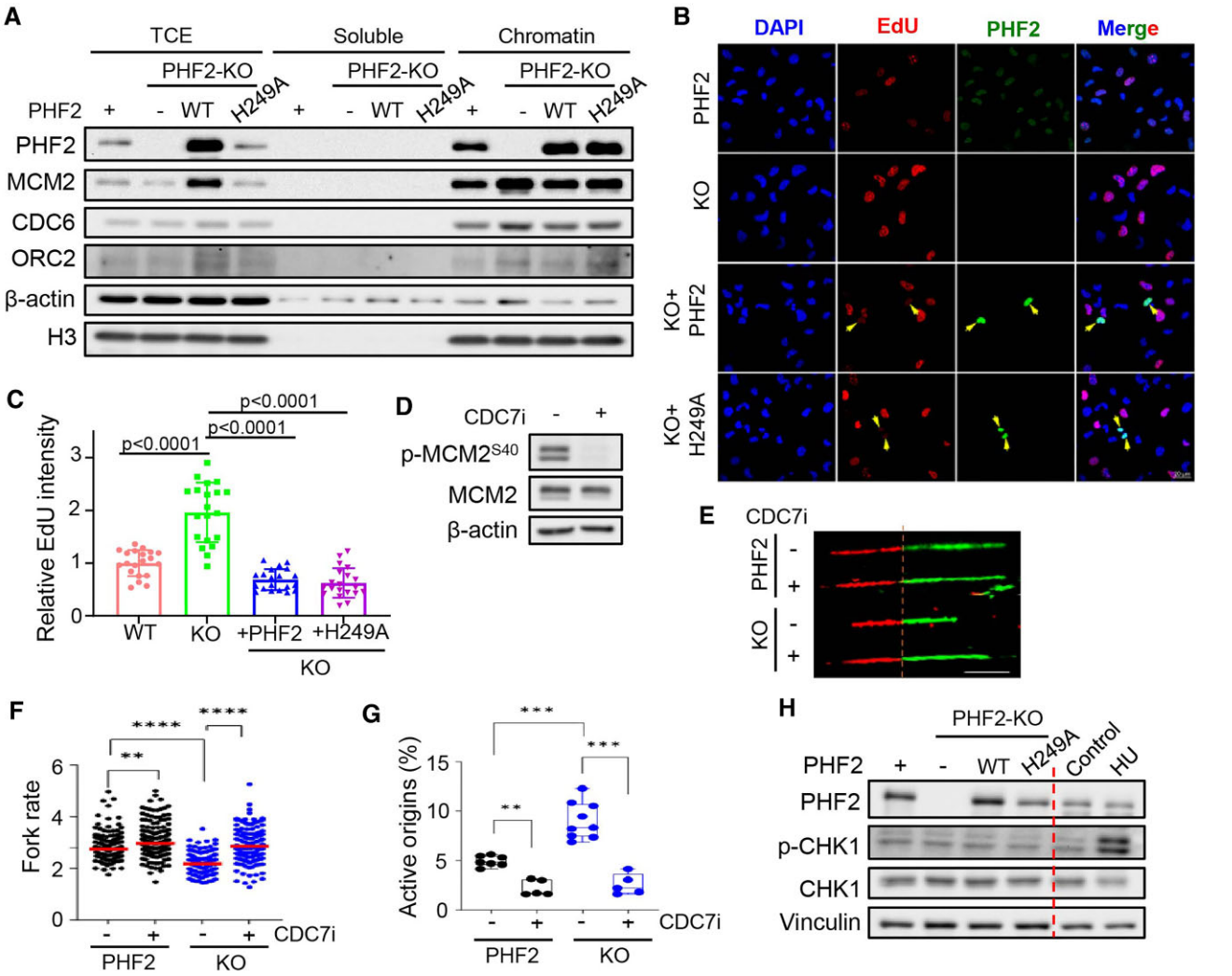

Figure 4. DNA replication defect in *PHF2* KO NSC is due to activation of dormant origins. (**A**) Western blot analysis of MCM2, CDC6, and ORC2 levels in the total cell extracts, soluble extracts, and chromatin extracts isolated from *PHF2* intact, *PHF2* KO, *PHF2* KO + PHF2, and *PHF2* KO + H249A mouse NSCs. PHF2 serves as positive control. β-actin and H3 serve as markers for the soluble and chromatin extracts, respectively. (**B, C**) Representative images and quantification of EdU labelling in *PHF2* intact, *PHF2* KO, *PHF2* KO + PHF2 and *PHF2* KO + H249A mouse NSCs. PHF2 overexpressing cells are indicated by the yellow arrows. Scale bar: 20 μm. (**D**) Western blot analysis of p-MCM2^{S40} and MCM2 levels in mouse NSCs with or without PHA-767491 treatment (60μM, 8hrs). (**E–G**) WT or *PHF2* KO mouse NSCs were pre-treated with or without 60μM PHA-767491 for 8 hours, and then labeled with CldU and IdU before cell harvesting. Fork rate was measured for individual replication forks presented in a scatterplot (F). Representative images of single DNA fibers are shown in (E). Scale bar, 10 μm. $n > 125$. % of active origins for individual replication forks presented in a scatterplot (G) ($n > 5$). (**H**) Western blot analysis of p-CHK1 and CHK1 levels in *PHF2* intact, *PHF2* KO, *PHF2* KO + PHF2, and *PHF2* KO + H249A mouse NSCs. HU treatment (3mM, 2hrs) serves as a positive control for p-CHK1 levels. PHF2 and vinculin serve as positive and loading controls, respectively.

RAD21, STAG1 and STAG2 in *PHF2* KO mouse NSC, and found that these were not visibly changed relative to *PHF2* intact cells (Figure 5G). However, we found decreased RAD21 occupancy on the promoters of a subset of PHF2/RAD21 co-bound genes in *PHF2* KO mouse NSC by using RAD21 ChIP-qPCR analysis (Figure 5H, I). Our collective data support the view that PHF2 facilitates RAD21 binding to PHF2/RAD21 co-bound sites, which are enriched for CTCF and epigenomic features that resemble efficient, active replication origins.

PHF2 KO mouse NSCs show weakened TADs at PHF2/RAD21 co-bound regions

The link between PHF2/RAD21 co-bound regions and CTCF prompted us to ask if PHF2 may influence TADs and chromatin loops, which can directly affect DNA replication (45,46). While TADs are domains of chromatin that make contacts with themselves at a higher rate than their surrounding chromatin (appear as triangles on a Hi-C map), chromatin loops are defined as two genomic regions that interact at a high frequency with one another (appear as dots/points on a Hi-C map). To this end, we prepared Hi-C libraries using *PHF2* KO and intact mouse NSC. Although *PHF2* KO did not affect TADs across the genome adversely (Figure 6A, B), we found that the PHF2/RAD21 co-bound regions can act as boundaries to separate adjacent domains (Figure 6C). We also calculated the fraction of co-bound, PHF2-only and RAD21-only peaks that overlap with TADs. Notably, the co-bound sites have the largest fraction of TADs (~0.55 compared to ~0.26 for PHF2-only and ~0.18 for RAD21-only) (Figure 6D). Moreover, we found that the insulation

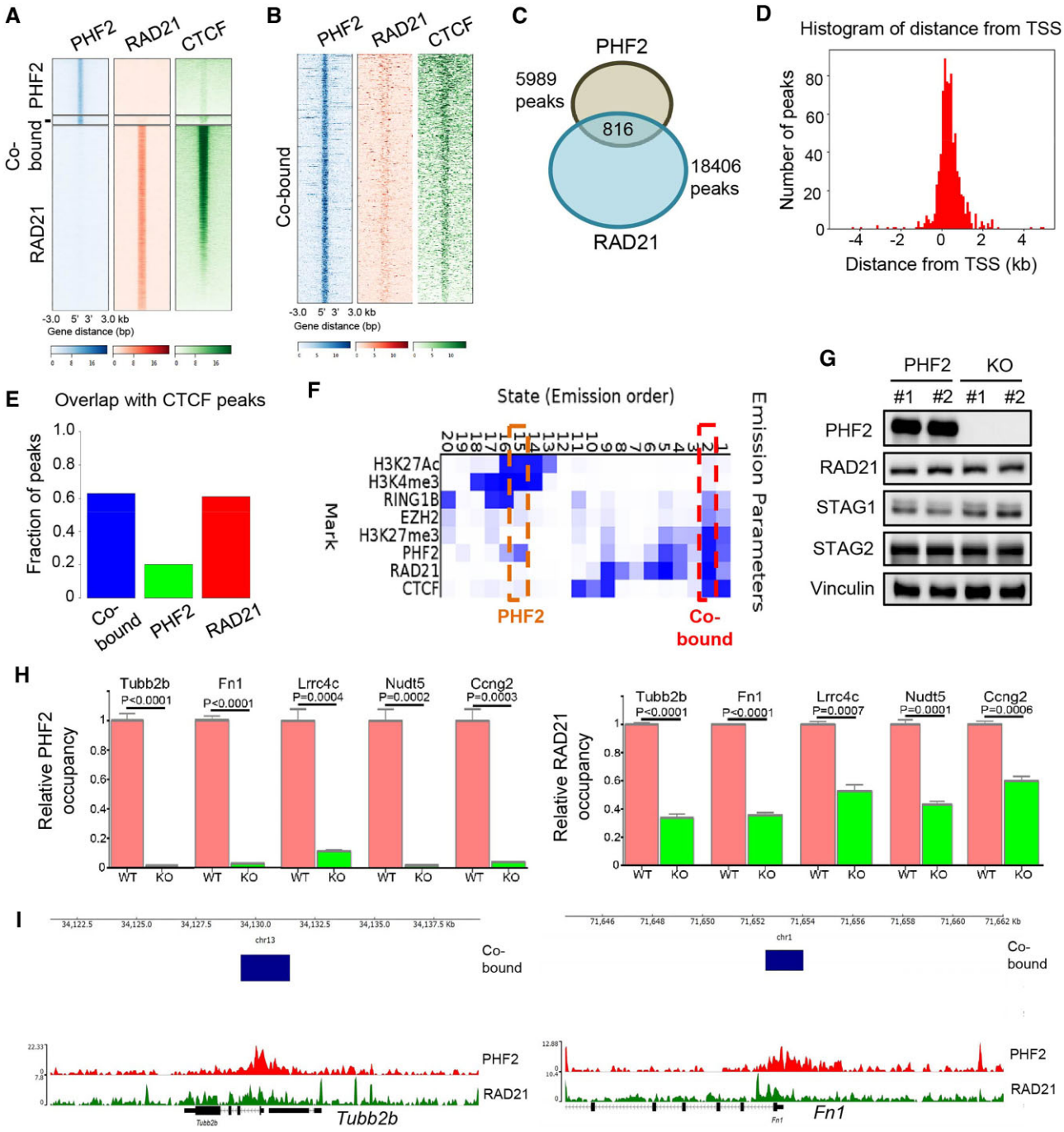

Figure 5. PHF2 facilitates RAD21 binding to PHF2/RAD21 co-bound sites, which are CTCF-enriched and resemble efficient replication origins. **(A, B)** Heatmaps indicating the PHF2-only, PHF2/RAD21 co-bound, and RAD21-only clusters and their CTCF binding profiles. (**C**) Overlap between PHF2 and RAD21 peaks in mouse NSCs, representing 816 co-bound peaks. (**D**) Histogram plot for the distance to TSS for all PHF2/RAD21 co-bound peaks. (**E**) Bar plot displaying the overlaps of co-bound, PHF2-only and RAD21-only peaks with CTCF peaks. All bars are represented as fractions of the total peaks in each category. (**F**) ChromHMM chromatin segment analysis representing emission states with differential enrichment profiles for PHF2, RAD21, CTCF, RING1B, EZH2, H3K27me3, H3K27Ac and H3K4me3. (**G**) Western blot analysis of RAD21, STAG1, and STAG2 in WT and *PHF2* KO mouse NSCs. PHF2 and vinculin serve as positive and loading controls, respectively. (**H**) ChIP-qPCR analysis of PHF2 and RAD21 occupancy at the promoters of *Tubb2b*, *Fn1*, *Lrrc4c*, *Nudt5* and *Ccng2* from WT and *PHF2* KO mouse NSCs. The fold-change was normalized to WT control. Two-sided *t*-test. (**I**) IGV browser view of PHF2 and RAD21 ChIP-seq peaks at the promoters of *Tubb2b* and *Fn1*.

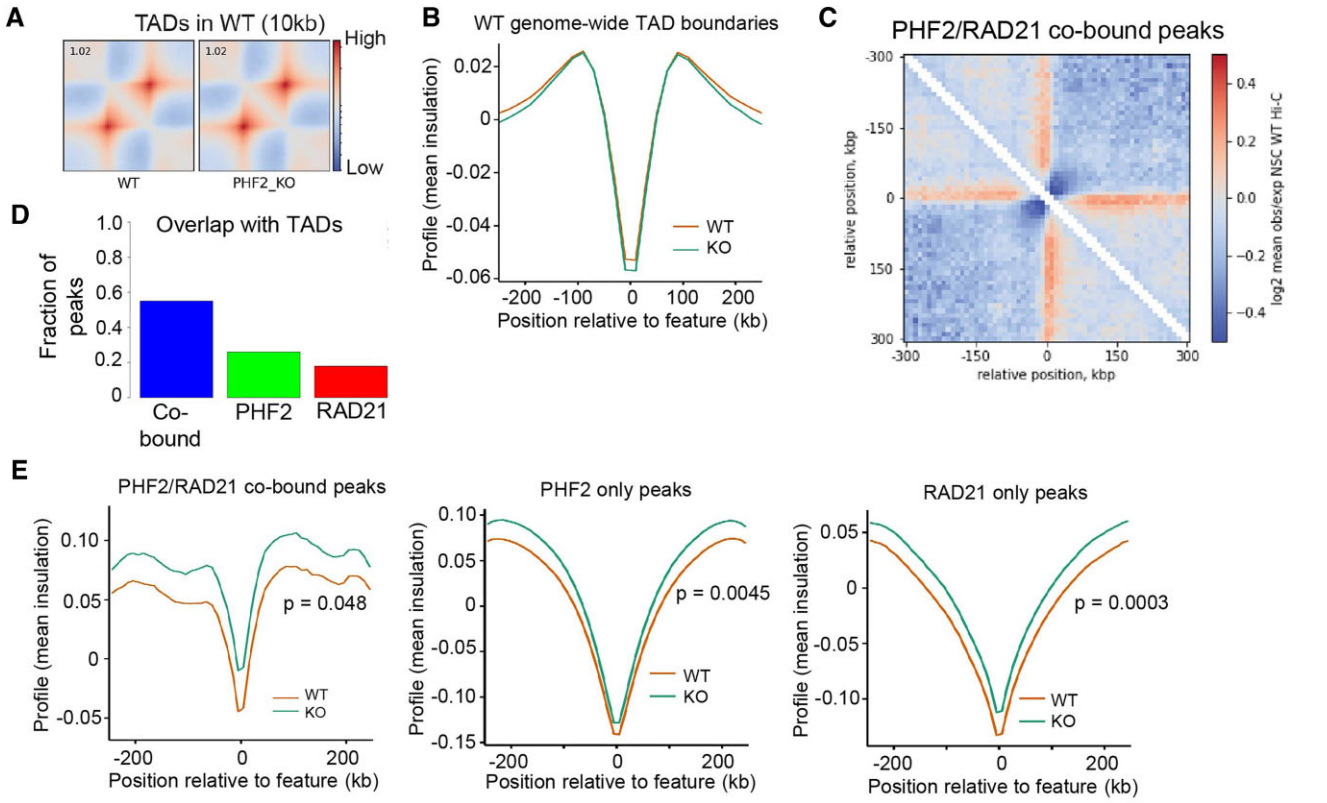

Figure 6. *PHF2* KO mouse NSCs show weakened TADs at PHF2/RAD21 co-bound regions. (**A**) Pileup plots of Hi-C signal on TADs for both WT and *PHF2* KO mouse NSCs. Value of central pixel was displayed. 10 kilobase resolution of the Hi-C data was used to plot the enrichment of interactions. (**B**) Average profile of insulation score of genome-wide TAD boundaries before and after *PHF2* KO. (**C**) Pileup plots showing local interaction, relative to randomize average genome wide interactions, around the PHF2/RAD21 co-bound regions using Hi-C data from mouse NSC. (**D**) Bar plot displaying the overlaps of co-bound, PHF2-only and RAD21-only peaks with TADs. All bars are represented as fractions of the total peaks in each category. (**E**) Average profile of insulation score in PHF2/RAD21 co-bound, PHF2-only, and RAD21-only peaks with and without *PHF2* KO.

strength decreased at PHF2/RAD21 co-bound, PHF2-only, and RAD21-only peaks upon *PHF2* KO (Figure 6E). Given that the co-bound but not PHF2-only sites have higher enrichment of CTCF and TADs, this supports the view that *PHF2* depletion may weaken TADs that are associated with PHF2/RAD21/CTCF co-occupancy.

We also examined changes in overall DNA loops upon *PHF2* loss. In our Hi-C dataset, 10 817 and 12 551 loops were identified in WT and *PHF2* KO mouse NSC, respectively. There were 3113 significantly downregulated loops (~24.8%) and 4516 significantly upregulated loops (~36%) in *PHF2* KO versus WT mouse NSC (Supplementary Figure S5A). We found that the insulation strength also decreased at anchors of downregulated loops (Supplementary Figure S5B). Moreover, there was a trend towards greater depletion of loops that coincide with PHF2/RAD21 co-bound peaks (correspond to 422 co-bound genes) when compared to PHF2-only peaks (correspond to 1180 PHF2-only genes), suggesting that *PHF2* loss may also disrupt chromatin loops (Supplementary Figure S5C, D). In contrast, we identified only 60 differential compartments, and the compartment switches are not very drastic. Since the compartment switches can affect replication timing, this finding is consistent with minor effects on global TAD boundaries in *PHF2* KO NSC. We conclude that *PHF2* depletion may result in the weakening of TADs and chromatin loops in RAD21-dependent and -independent manners.

The PHF2/RAD21 complex does not contribute towards gene regulation in mouse NSC

Does the PHF2/RAD21 complex control gene transcription by regulating chromatin loops in mouse NSC? To address this, we compared genes that were downregulated upon *PHF2* loss (focusing on those with evidence of PHF2 binding at their promoters) vs those that were commonly downregulated upon *PHF2* and *RAD21* depletion (while also considering the accompanied DNA loop losses). RNA-Seq followed by Gene Ontology analysis of *PHF2* KO mouse NSC showed downregulation of genes that were enriched in pathways including extracellular matrix and regulation of monoatomic ion transport pathways, as well as upregulation of genes that were enriched in pathways including tissue and embryonic morphogenesis (Figure 7A). Next, we intersected these differentially expressed genes upon *PHF2* KO with those that harboured PHF2 binding sites at their promoters from a public dataset of mouse NSC (23). This integrative analysis led to 51 downregulated PHF2 target genes which were enriched in pathways including gonadotrophin-releasing hormone neuronal migration to the hypothalamus, and 52 upregulated PHF2 target genes which were enriched in pathways including regeneration (Figure 7B, C). On the other hand, Gene Ontology analysis of genes associated with the depletion of DNA loops in *PHF2* KO NSC were enriched in pathways, including cell morphogenesis and synapse organization, and only 12 genes in this group were commonly downregulated by

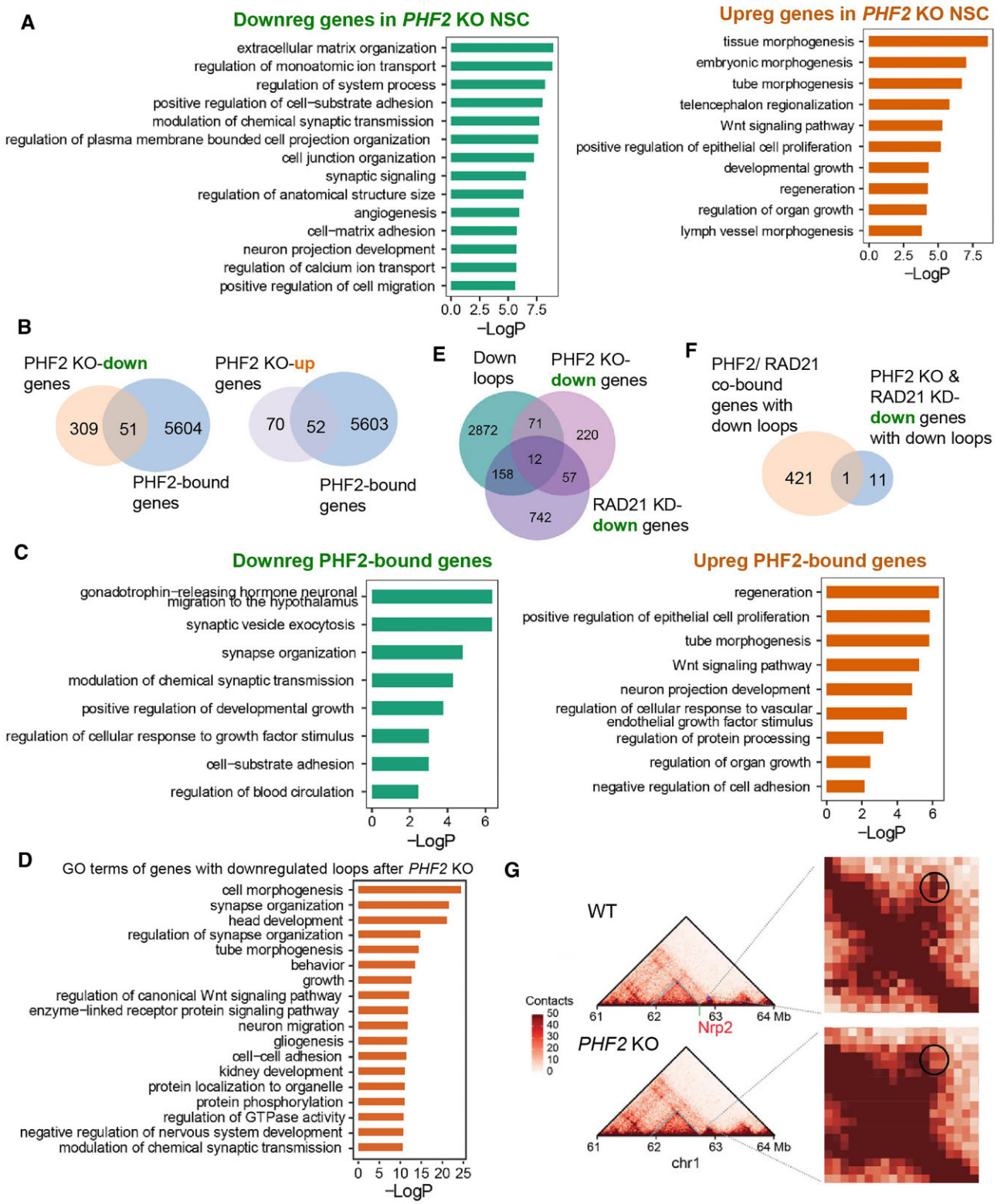

Figure 7. The PHF2/RAD21 complex does not contribute towards gene regulation in mouse NSC. (**A**) Gene Ontology (GO) analysis of downregulated and upregulated genes upon *PHF2* KO in mouse NSC (FC ≥ 1.5, adjusted *P* value < 0.05). (**B**) Venn diagrams showing the number of overlapped genes between the differentially expressed genes upon *PHF2* KO and genes containing PHF2 occupancy at their promoters. (**C**) GO analysis with common genes from (B). (**D**) GO analysis of genes with downregulated chromatin loops upon *PHF2* KO. (**E**) Venn diagram showing the overlap between downregulated loops-enriched genes, *PHF2* KO-associated downregulated genes, and *RAD21* KD-associated downregulated genes. (**F**) Venn diagram showing the overlap between Supplementary Figure S5D and (E). (**G**) Pyramid chromatin contact matrix heatmaps were shown around *Nrp2* that survived the overlap in (F). A zoom in of the region-of-interest marking loss of 'corner peak' for *Nrp2* in *PHF2* KO mouse NSC is shown on the right.

PHF2 and *RAD21* depletion (Figure 7D, E). Notably, only one gene (*Nrp2*) survived if we were to consider the presence of PHF2/RAD21 co-occupancy on the promoters of these genes (Figure 7F, G). The *Nrp2* gene encodes for a semaphorin receptor, which promotes dendritic growth and branching during adult hippocampal neurogenesis (47), and its downregulation is unlikely to account for DNA replication defect of *PHF2* KO mouse NSC. Taken together, we find that the PHF2/RAD21 complex does not contribute towards gene regulation in mouse NSC.

Human cortical organoids reveal that PHF2 promotes NSC proliferation in a histone demethylase-independent manner

The above data indicate that PHF2 mediates DNA replication via cohesin in a histone demethylase-independent manner in mouse NSC, with little impact on gene regulation. Last, we sought to address if the histone demethylase activity of PHF2 is required for NSC proliferation by using wildtype, *PHF2* KO, *PHF2* KO + PHF2 or *PHF2* KO + H249A embryonic stem cells for the generation of cortical spheroids (Supplementary Figure S6A-D). *PHF2* loss significantly decreased the size of the cortical organoids, which was rescued by the re-expression of either PHF2 or H249A (Figure 8A, B). This tracked closely with the number of NSC ($Sox2^+$), proliferating cells ($Ki67^+$) and neuroepithelial structures ($ZO\text{-}1^+$) (Figure 8C–H). We also showed that these cellular phenotypes correlate with the % of γH2AX positive cells (as an indirect reporter for DNA replication defect) (Supplementary Figure S6E, F). These rescue experiments establish a link between PHF2-mediated DNA replication and NSC proliferation, which does not require PHF2's histone demethylase activity.

Discussion

Our collective data supports the view that PHF2 regulates DNA replication and NSC proliferation in a histone demethylase-independent manner. The ability of PHF2's PHD domain to recognize H3K4me2/3 histone marks (19) may allow PHF2 to act as a topological accessory for cohesin recruitment to PHF2/RAD21 co-bound sites, which are characterized by CTCF and TAD enrichment, and efficient, active replication origin-associated epigenomic features. Accordingly, *PHF2* KO weakens TAD boundaries (and chromatin loops) at PHF2/RAD21 co-bound regions due to reduced RAD21 occupancy. These topological defects activate dormant replication origins that in turn impair DNA replication in NSC, which may be explained by two plausible models as depicted in our Graphical Abstract. In Model 1, we speculate that PHF2 promotes TAD formation and hence high-efficiency, active replication origins at the co-bound regions. Upon *PHF2* loss, the weakening of TADs (and reduced chromatin loops) inactivates the high-efficiency, active replication origins, leading to the activation of backup dormant origins for DNA replication which may in turn deplete nucleotides. This model would corroborate with the view that cohesin can positively regulate DNA replication by mediating loop anchors that restrict the locations of replication origins or organizing chromatin loops at DNA replication factories (45,46). In Model 2, we speculate that PHF2 promotes TAD formation which represses dormant replication origins at the co-bound regions. Upon *PHF2* loss, the weakening of TADs (and reduced chromatin loops) directly activates the dormant replication origins. This model would align with the report by Wu *et al.* (12) demonstrating a role of RAD21 (and cohesin) in repressing dormant origin firing in chromatin loops to control replication timing in human K562 and mouse embryonic stem cells. We favor Model 1 given that the PHF2/RAD21 co-bound sites resemble high-efficiency, active origins and this can account for how a small number of co-bound sites can influence global DNA replication.

The genomic occupancy of cohesin complex can be directly or indirectly regulated by epigenetic regulators and transcription factors. For example, BRD4 interacts with NIPBL (a cohesin agonist) to regulate NIPBL occupancy on chromatin, which is important for the maintenance of TADs for the transcriptional regulation of genes necessary for neural crest differentiation (48). In another instance, the histone methyltransferase SETDB1 regulates the genomic occupancy of cohesin complex at the DiSC (Domains involving SETDB1 & Cohesin, and devoid of H3K9me3 marks) regions, thereby contributing to the maintenance of TADs and chromatin loop architectures in ESCs (49). Notably, both BRD4 and SETDB1 regulate cell fates by maintaining DNA topologies for gene regulation in the aforementioned examples (48,49), which is distinct from our finding that genome topology changes upon *PHF2* loss unlikely contribute towards gene regulation in mouse NSC. Interestingly, ZBTB transcription factors, including ZBTB21, can interact with cohesin at gene promoters, where they insulate small-scale 3D chromatin interactions (18). ZBTB21 depletion reduces chromatin binding of cohesin and affects 3D chromatin interaction of ZBTB21-bound promoters. Thus, our mechanistic investigation of PHF2 shows similarities with that reported for ZBTB21 in these aspects.

In contrast to PHF2's canonical role as an epigenetic regulator that modulates gene expression through its histone demethylase activity (23,50), we have identified a non-canonical role of PHF2 in promoting mouse NSC proliferation. Not surprisingly, the lysine demethylase-independent function of other histone demethylases have also been reported. For instance, Kdm5/Lid regulates the pairing of homologous centromeres to facilitate synaptonemal complex formation for crossover during the prophase of meiosis I independently of its demethylase activity in *Drosophila* (51). In cancer, the lysine demethylase LSD1 binds and blocks the dimerization of tumor suppressor FBXW7, leading to increased self-ubiquitination and protein degradation (52). The demethylase activity of LSD1 is dispensable for the destabilization of FBXW7 (52).

Dysregulated DNA replication in NSC can lead to brain development defects and neurological disorders. For instance, neuroepithelial cells (a distinct type of NSC population which drives neurogenesis until E10.5) exhibit short G1 phase that is attributed to increased MCM loading and replication origin activation (53). Disturbing DNA replication licensing by Geminin ablation in neuroepithelial cells impairs DNA replication, increases replication stress, and induces microcephaly phenotypes (53). In another example, autism spectrum disorder-associated human neural progenitor cells (that are generated from induced pluripotent stem cells of autism spectrum disorder patients) exhibit accelerated S phase progression and increased replication forks within each loci, which leads to replication stress and DNA damage preferentially at actively transcribing long genes (54). This

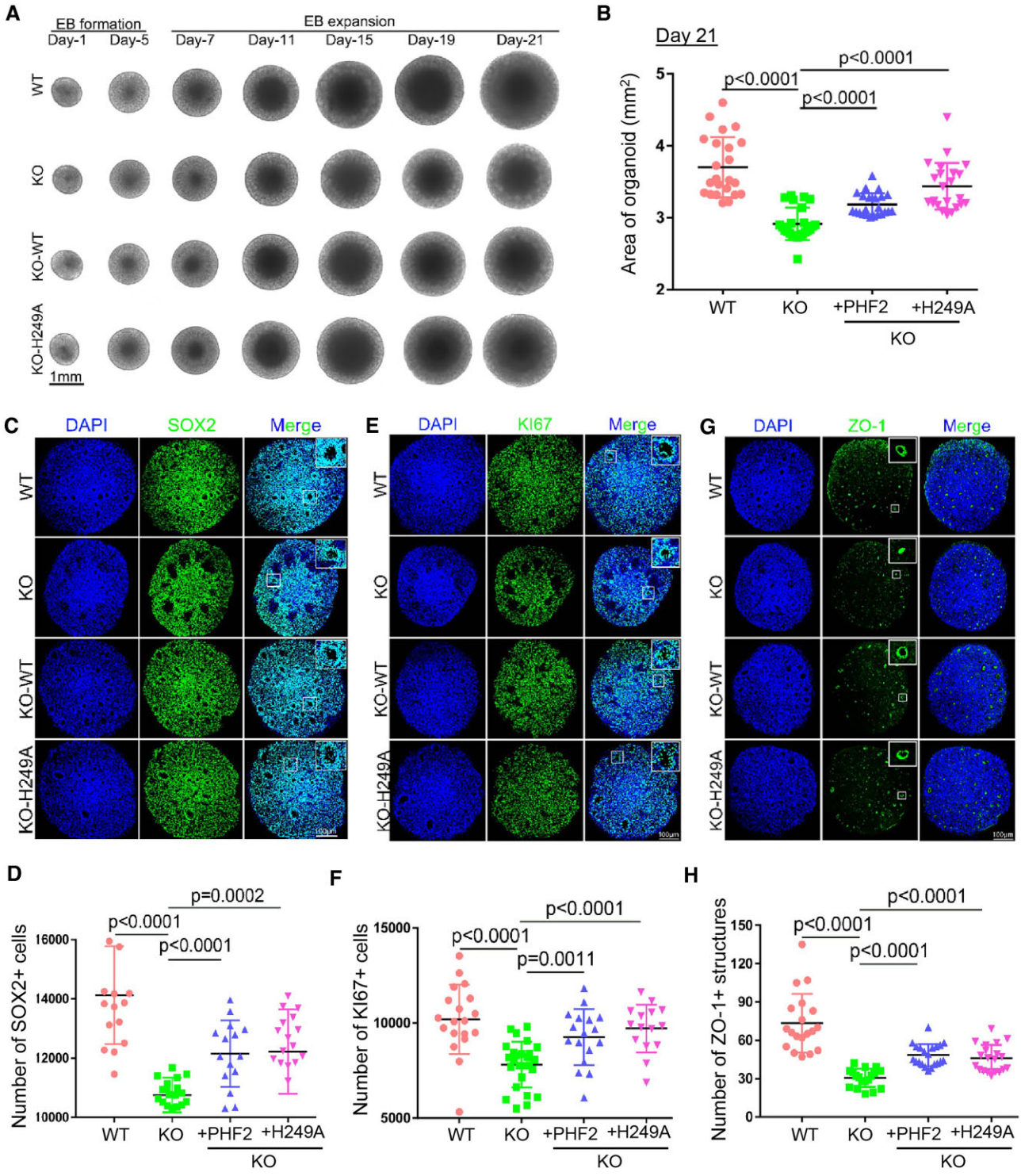

Figure 8. Human cortical organoids reveal that PHF2 promotes NPC proliferation in a histone demethylase-independent manner. (**A**) Brightfield images of cortical spheroids at the indicated time points during the course of differentiation. (**B**) Quantification of spheroid areas in *PHF2* intact, *PHF2* KO, *PHF2* KO + PHF2 and *PHF2* KO + H249A spheroids ($n = 24$). **(C, D)** Confocal images and quantification of the number of NSCs ($SOX2^+$) in *PHF2* intact, *PHF2* KO, *PHF2* KO + PHF2, and *PHF2* KO + H249A spheroids ($n = 6$). (**E, F**) Confocal images and quantification of the number of proliferating NSCs ($Ki67^+$) in *PHF2* intact, *PHF2* KO, *PHF2* KO + PHF2 and *PHF2* KO + H249A spheroids ($n = 6$). (**G, H**) Confocal images and quantification of the number of lumen ($ZO\text{-}1^+$) in *PHF2* intact, *PHF2* KO, *PHF2* KO + PHF2 and *PHF2* KO + H249A spheroids ($n = 6$). Box shows the magnified view of neuroepithelial structure.

precipitates into replication-transcription conflicts that downregulate genes involved in cell adhesion and migration. In conclusion, we have discovered a non-canonical role of PHF2 in regulating mouse NSC proliferation by mediating DNA replication via cohesin. Our study may motivate deeper mechanistic investigation of how PHF2 would regulate genome topology that can impact the function of other tissue stem cells.

Data availability

All data, supplemental data, and data in repositories are available. Raw data from RNA-Seq analysis of mouse NSC with or without *PHF2* knockout (GSE225438), RNA-Seq analysis of mouse NSC with or without *RAD21* knockdown (GSE225608), and Hi-C data mouse NSC with or without *PHF2* knockout (GSE243810). Raw data from BioID-mass spectrometry analysis can be accessed in the ProteomeXchange via accession code PXD040515.

Supplementary data

Supplementary Data are available at NAR online.

Acknowledgements

We thank Toshio Suda and Sriram Sridharan from the Cancer Science Institute, National University of Singapore (NUS) and Tuck Wah Soong from NUS for invaluable discussion; Shu Ying Lee from the Confocal Microscopy Unit at Yong Loo Lin School of Medicine for microscopy support; as well as Kagistia Hana Utami and Mahmoud A Pouladi for advice with organoid experiments.

Author contributions: D.S.T.O. designed and guided the research; J.F., Y.H.C., Y.L., N.O.C., G.A.R.E.E., J.H., E.X.Y.T., K.L., Z.Z., E.M.S., C.N.J.Y., O.G., H.Y.C., J.Y.L., K.C.C. and C.F.C. performed research. Y.Z., T.S., J.T. and Y.L. analyzed Hi-C, ChIP-Seq public datasets and ChromHMM. O.G. analyzed bulk RNA-sequencing and public datasets. Z.J.K, Z.S.C. and S.N. assisted with human cortical organoids. L.C.W., Y.T.L., T.Z. and R.M.S. performed mass spectrometry analysis. V.T., R.T. and S.L. provided intellectual contributions. D.S.T.O., Y.H.C. and J.F. wrote the manuscript.

Funding

National University of Singapore Start-up (D.S.T.O.); NUS President's Assistant Professorship (D.S.T.O.); Ministry of Education (Singapore) Tier 2 [MOE-T2EP30121-0011 to D.S.T.O.]. Funding for open access charge: Ministry of Education (Singapore) Tier 2 [MOE-T2EP30121-0011].

Conflict of interest statement

None declared.

References

1. Nasmyth,K. and Haering,C.H. (2009) Cohesin: its roles and mechanisms. *Annu. Rev. Genet.*, **43**, 525–558.
2. Litwin,I., Pilarczyk,E. and Wysocki,R. (2018) The emerging role of cohesin in the DNA damage response. *Genes (Basel)*, **9**, 581.
3. Waldman,T. (2020) Emerging themes in cohesin cancer biology. *Nat. Rev. Cancer*, **20**, 504–515.
4. Peters,J.M., Tedeschi,A. and Schmitz,J. (2008) The cohesin complex and its roles in chromosome biology. *Genes Dev.*, **22**, 3089–3114.
5. Wutz,G., Varnai,C., Nagasaka,K., Cisneros,D.A., Stocsits,R.R., Tang,W., Schoenfelder,S., Jessberger,G., Muhar,M., Hossain,M.J., *et al.* (2017) Topologically associating domains and chromatin loops depend on cohesin and are regulated by CTCF, WAPL, and PDS5 proteins. *EMBO J.*, **36**, 3573–3599.
6. Hansen,A.S., Cattoglio,C., Darzacq,X. and Tjian,R. (2018) Recent evidence that TADs and chromatin loops are dynamic structures. *Nucleus*, **9**, 20–32.
7. Li,Y., Haarhuis,J.H.I., Sedeno Cacciatore,A., Oldenkamp,R., van Ruiten,M.S., Willems,L., Teunissen,H., Muir,K.W., de Wit,E., Rowland,B.D., *et al.* (2020) The structural basis for cohesin-CTCF-anchored loops. *Nature*, **578**, 472–476.
8. Nora,E.P., Goloborodko,A., Valton,A.L., Gibcus,J.H., Uebersohn,A., Abdennur,N., Dekker,J., Mirny,L.A. and Bruneau,B.G. (2017) Targeted degradation of CTCF decouples local insulation of chromosome domains from genomic compartmentalization. *Cell*, **169**, 930–944.
9. Schwarzer,W., Abdennur,N., Goloborodko,A., Pekowska,A., Fudenberg,G., Loe-Mie,Y., Fonseca,N.A., Huber,W., Haering,C.H., Mirny,L., *et al.* (2017) Two independent modes of chromatin organization revealed by cohesin removal. *Nature*, **551**, 51–56.
10. Rao,S.S.P., Huang,S.C., St Hilaire,B.G., Engreitz,J.M., Perez,E.M., Kieffer-Kwon,K.R., Sanborn,A.L., Johnstone,S.E., Bascom,G.D., Bochkov,I.D., *et al.* (2017) Cohesin loss eliminates all loop domains. *Cell*, **171**, 305–320.
11. Marchal,C., Sima,J. and Gilbert,D.M. (2019) Control of DNA replication timing in the 3D genome. *Nat. Rev. Mol. Cell Biol.*, **20**, 721–737.
12. Wu,J.C., Liu,Y., Zhangding,Z., Liu,X.H., Ai,C., Gan,T.T., Liang,H.X., Guo,Y.F., Chen,M., Liu,Y.Y., *et al.* (2023) Cohesin maintains replication timing to suppress DNA damage on cancer genes. *Nat. Genet.*, **55**, 1347–1358.
13. Hu,Y. and Stillman,B. (2023) Origins of DNA replication in eukaryotes. *Mol. Cell*, **83**, 352–372.
14. Pope,B.D., Ryba,T., Dileep,V., Yue,F., Wu,W., Denas,O., Vera,D.L., Wang,Y., Hansen,R.S., Canfield,T.K., *et al.* (2014) Topologically associating domains are stable units of replication-timing regulation. *Nature*, **515**, 402–405.
15. Emerson,D.J., Zhao,P.A., Cook,A.L., Barnett,R.J., Klein,K.N., Saulebekova,D., Ge,C., Zhou,L., Simandi,Z., Minsk,M.K., *et al.* (2022) Cohesin-mediated loop anchors confine the locations of human replication origins. *Nature*, **606**, 812–819.
16. Courbet,S., Gay,S., Arnoult,N., Wronka,G., Anglana,M., Brison,O. and Debatisse,M. (2008) Replication fork movement sets chromatin loop size and origin choice in mammalian cells. *Nature*, **455**, 557–560.
17. Li,Y., Xue,B., Zhang,M., Zhang,L., Hou,Y., Qin,Y., Long,H., Su,Q.P., Wang,Y., Guan,X., *et al.* (2021) Transcription-coupled structural dynamics of topologically associating domains regulate replication origin efficiency. *Genome Biol.*, **22**, 206.
18. Wang,R., Xu,Q.Q., Wang,C.L., Tian,K., Wang,H. and Ji,X. (2023) Multiomic analysis of cohesin reveals that ZBTB transcription factors contribute to chromatin interactions. *Nucleic Acids Res.*, **51**, 6784–6805.
19. Wen,H., Li,J.Z., Song,T.J., Lu,M., Kan,P.Y., Lee,M.G., Sha,B.D. and Shi,X.B. (2010) Recognition of histone H3K4 trimethylation by the plant homeodomain of PHF2 modulates histone demethylation. *J. Biol. Chem.*, **285**, 9322–9326.
20. Okuno,Y., Ohtake,F., Igarashi,K., Kanno,J., Matsumoto,T., Takada,I., Kato,S. and Imai,Y. (2013) Epigenetic regulation of adipogenesis by PHF2 histone demethylase. *Diabetes*, **62**, 1426–1434.
21. Kim,H.J., Park,J.W., Lee,K.H., Yoon,H., Shin,D.H., Ju,U.I., Seok,S.H., Lim,S.H., Lee,Z.H., Kim,H.H., *et al.* (2014) Plant homeodomain finger protein 2 promotes bone formation by demethylating and activating Runx2 for osteoblast differentiation. *Cell Res.*, **24**, 1231–1249.

22. Hata,K., Takashima,R., Amano,K., Ono,K., Nakanishi,M., Yoshida,M., Wakabayashi,M., Matsuda,A., Maeda,Y., Suzuki,Y., *et al.* (2013) Arid5b facilitates chondrogenesis by recruiting the histone demethylase Phf2 to Sox9-regulated genes. *Nat. Commun.*, **4**, 2850.
23. Pappa,S., Padilla,N., Lacobucci,S., Vicioso,M., de la Campa,E.A., Navarro,C., Marcos,E., de la Cruz,X. and Martinez-Balbas,M.A. (2019) PHF2 histone demethylase prevents DNA damage and genome instability by controlling cell cycle progression of neural progenitors. *Proc. Nat. Acad. Sci. U.S.A.*, **116**, 19464–19473.
24. Jeong,D.W., Park,J.W., Kim,K.S., Kim,J., Huh,J., Seo,J., Kim,Y.L., Cho,J.Y., Lee,K.W., Fukuda,J., *et al.* (2023) Palmitoylation-driven PHF2 ubiquitination remodels lipid metabolism through the SREBP1c axis in hepatocellular carcinoma. *Nat. Commun.*, **14**, 6370.
25. Ran,F.A., Hsu,P.D., Wright,J., Agarwala,V., Scott,D.A. and Zhang,F. (2013) Genome engineering using the CRISPR-Cas9 system. *Nat. Protoc.*, **8**, 2281–2308.
26. Pasca,A.M., Sloan,S.A., Clarke,L.E., Tian,Y., Makinson,C.D., Huber,N., Kim,C.H., Park,J.Y., O'Rourke,N.A., Nguyen,K.D., *et al.* (2015) Functional cortical neurons and astrocytes from human pluripotent stem cells in 3D culture. *Nat. Methods*, **12**, 671–678.
27. Tapia Del Fierro,A., Hamer,B., Benetti,N., Jansz,N., Chen,K., Beck,T., Vanyai,H., Gurzau,A.D., Daxinger,L., Xue,S., *et al.* (2023) SMCHD1 has separable roles in chromatin architecture and gene silencing that could be targeted in disease. *Nat. Commun.*, **14**, 5466.
28. Gao,Y., Duque-Wilckens,N., Aljazi,M.B., Moeser,A.J., Mias,G.I., Robison,A.J., Zhang,Y. and He,J. (2022) Impaired KDM2B-mediated PRC1 recruitment to chromatin causes defective neural stem cell self-renewal and ASD/ID-like behaviors. *iScience*, **25**, 103742.
29. Sher,F., Boddeke,E., Olah,M. and Copray,S. (2012) Dynamic changes in Ezh2 gene occupancy underlie its involvement in neural stem cell self-renewal and differentiation towards oligodendrocytes. *PLoS One*, **7**, e40399.
30. Halliwell,J.A., Gravells,P. and Bryant,H.E. (2020) DNA Fiber assay for the analysis of DNA replication progression in Human pluripotent stem cells. *Curr. Protoc. Stem Cell Biol.*, **54**, e115.
31. Mendez,J.S. and,B. (2000) Chromatin association of human origins recognition complex Cdc6, and minichromosome maintenance proteins during the cell cycle-assembly of prereplication complexes in late mitosis. *Mol. Cell. Biol.*, **20**, 8602–8612.
32. Durand,N.C., Shamim,M.S., Machol,I., Rao,S.S., Huntley,M.H., Lander,E.S. and Aiden,E.L. (2016) Juicer provides a one-click system for analyzing loop-resolution Hi-C experiments. *Cell Syst.*, **3**, 95–98.
33. Abdennur,N. and Mirny,L.A. (2020) Cooler: scalable storage for Hi-C data and other genomically labeled arrays. *Bioinformatics*, **36**, 311–316.
34. Roayaei Ardakany,A., Gezer,H.T., Lonardi,S. and Ay,F. (2020) Mustache: multi-scale detection of chromatin loops from Hi-C and Micro-C maps using scale-space representation. *Genome Biol.*, **21**, 256.
35. Flyamer,I.M., Illingworth,R.S. and Bickmore,W.A. (2020) Coolpup.Py: versatile pile-up analysis of hi-C data. *Bioinformatics*, **36**, 2980–2985.
36. van der Weide,R.H., van den Brand,T., Haarhuis,J.H.I., Teunissen,H., Rowland,B.D. and de Wit,E. (2021) Hi-C analyses with GENOVA: a case study with cohesin variants. *NAR Genom. Bioinform.*, **3**, lqab040.
37. Pattabiraman,D.R., Bierie,B., Kober,K.I., Thiru,P., Krall,J.A., Zill,C., Reinhardt,F., Tam,W.L. and Weinberg,R.A. (2016) Activation of PKA leads to mesenchymal-to-epithelial transition and loss of tumor-initiating ability. *Science*, **351**, aad3680.
38. Moiseeva,T.N., Yin,Y.D., Calderon,M.J., Qian,C.A., Schamus-Haynes,S., Sugitani,N., Osmanbeyoglu,H.U., Rothenberg,E., Watkins,S.C. and Bakkenist,C.J. (2019) An ATR and CHK1 kinase signaling mechanism that limits origin firing during unperturbed DNA replication. *Proc. Nat. Acad. Sci. U.S.A.*, **116**, 13374–13383.
39. Cheng,H.Z., Zhang,N.G. and Pati,D. (2020) Cohesin subunit RAD21: from biology to disease. *Gene*, **758**, 144966.
40. Perea-Resa,C., Bury,L., Cheeseman,I.M. and Blower,M.D. (2020) Cohesin removal reprograms gene expression upon mitotic entry. *Mol. Cell*, **78**, 127–140.
41. Singh,A.K., Chen,Q.R., Nguyen,C., Meerzaman,D. and Singer,D.S. (2023) Cohesin regulates alternative splicing. *Sci. Adv.*, **9**, eade3876.
42. Rodriguez-Acebes,S., Mourón,S. and Méndez,J. (2018) Uncoupling fork speed and origin activity to identify the primary cause of replicative stress phenotypes. *J. Biol. Chem.*, **293**, 12855–12861.
43. Jodkowska,K., Pancaldi,V., Rigau,M., Almeida,R., Fernández-Justel,J.M., Graña-Castro,O., Rodríguez-Acebes,S., Rubio-Camarillo,M., Pau,E.C.D., Pisano,D., *et al.* (2022) 3D chromatin connectivity underlies replication origin efficiency in mouse embryonic stem cells. *Nucleic Acids Res.*, **50**, 12149–12165.
44. Cayrou,C., Ballester,B., Peiffer,I., Fenoui,R., Coulombe,P., Andrau,J.C., van Helden,J. and Méchalil,M. (2015) The chromatin environment shapes DNA replication origin organization and defines origin classes. *Genome Res.*, **25**, 1873–1885.
45. Emerson,D.J., Zhao,P.Y.A., Cook,A.L., Barnett,R.J., Klein,K.N., Saulebekova,D., Ge,C.M., Zhou,L.D., Simandi,Z., Minsk,M.K., *et al.* (2022) Cohesin-mediated loop anchors confine the locations of human replication origins. *Nature*, **606**, 812–819.
46. Guillou,E., Ibarra,A., Coulon,V., Casado-Vela,J., Rico,D., Casal,I., Schwob,E., Losada,A. and Méndez,J. (2010) Cohesin organizes chromatin loops at DNA replication factories. *Genes Dev.*, **24**, 2812–2822.
47. Ng,T., Ryu,J.R., Sohn,J.H., Tan,T., Song,H.J., Ming,G.L. and Goh,E.L.K. (2013) Class 3 semaphorin mediates dendrite growth in adult newborn neurons through Cdk5/FAK pathway. *PLoS One*, **8**, e65572.
48. Linares-Saldana,R., Kim,W., Bolar,N.A., Zhang,H., Koch-Bojalad,B.A., Yoon,S., Shah,P.P., Karnay,A., Park,D.S., Luppino,J.M., *et al.* (2021) BRD4 orchestrates genome folding to promote neural crest differentiation. *Nat. Genet.*, **53**, 1480–1492.
49. Warrier,T., El Farran,C., Zeng,Y., Ho,B.S.Q., Bao,Q., Zheng,Z.H., Bi,X., Ng,H.H., Ong,D.S.T., Chu,J.J.H., *et al.* (2022) SETDB1 acts as a topological accessory to Cohesin via an H3K9me3-independent, genomic shunt for regulating cell fates. *Nucleic. Acids. Res.*, **50**, 7326–7349.
50. Alonso-de Vega,I., Paz-Cabrera,M.C., Rother,M.B., Wiegant,W.W., Checa-Rodriguez,C., Hernandez-Fernaud,J.R., Huertas,P., Freire,R., van Attikum,H. and Smits,V.A.J. (2020) PHF2 regulates homology-directed DNA repair by controlling the resection of DNA double strand breaks. *Nucleic. Acids. Res.*, **48**, 4915–4927.
51. Zhaunova,L., Ohkura,H. and Breuer,M. (2016) Kdm5/Lid regulates chromosome architecture in meiotic prophase I independently of its histone demethylase activity. *PLoS Genet.*, **12**, e1006241.
52. Lan,H., Tan,M., Zhang,Q., Yang,F., Wang,S., Li,H., Xiong,X. and Sun,Y. (2019) LSD1 destabilizes FBXW7 and abrogates FBXW7 functions independent of its demethylase activity. *Proc. Natl. Acad. Sci. U.S.A.*, **116**, 12311–12320.
53. Kalogeropoulou,A., Mougkogianni,M., Iliadou,M., Nikolopoulou,E., Flordelis,S., Kanellou,A., Arbi,M., Nikou,S., Nieminuszczy,J., Niedzwiedz,W., *et al.* (2022) Intrinsic neural stem cell properties define brain hypersensitivity to genotoxic stress. *Stem Cell Rep.*, **17**, 1395–1410.
54. Wang,M., Wei,P.C., Lim,C.K., Gallina,I.S., Marshall,S., Marchetto,M.C., Alt,F.W. and Gage,F.H. (2020) Increased neural progenitor proliferation in a hiPSC model of autism induces replication stress-associated genome instability. *Cell Stem Cell*, **26**, 221–233.

Received: October 19, 2023. **Revised:** April 15, 2024. **Editorial Decision:** May 9, 2024. **Accepted:** May 15, 2024